ACS APPLIED MATERIALS & INTERFACES

www.acsami.org

Research Article

Highly Luminescent, Stable, and Red-Emitting $CsMg_xPb_{1-x}I_3$ Quantum Dots for Dual-Modal Imaging-Guided Photodynamic Therapy and Photocatalytic Activity

Girum Getachew, Chiranjeevi Korupalli, Akash S. Rasal, Worku Batu Direrse, Mochamad Z. Fahmi, and Jia-Yaw Chang*

Cite This: *ACS Appl. Mater. Interfaces* 2022, 14, 278−296

Read Online

ACCESS | Metrics & More | Article Recommendations | Supporting Information

ABSTRACT: In this study, for the first time, red-emitting $CsMg_xPb_{1-x}I_3$ quantum dots (QDs) are prepared by doping with magnesium (Mg) ions via the one-pot microwave pyrolysis technique. The X-ray diffraction and X-ray photoelectron spectroscopy results have confirmed partial substitution of Pb^{2+} by Mg^{2+} inside the $CsPbI_3$ framework. The as-synthesized $CsMg_xPb_{1-x}I_3$ QDs have exhibited excellent morphology, higher quantum yield (upto ∼89%), better photostability and storage stability than undoped $CsPbI_3$. Next, the bioavailability of as-synthesized hydrophobic $CsMg_xPb_{1-x}I_3$ QDs is improved by encapsulating them into gadolinium-conjugated pluronic 127 (PF127-Gd) micelles through hydrophobic interactions (PQD@Gd). The optical properties of perovskite quantum dots (PQDs) and the presence of Gd could endow the PQD@Gd with fluorescence imaging, magnetic resonance imaging (MRI), and phototherapeutic properties. Accordingly, the MRI contrasting effects of PQD@Gd nanoagents are demonstrated by employing T_1 and T_2 studies, which validated that PQD@Gd nanoagents had superior MR contrasting effect with a r_2/r_1 ratio of 1.38. In vitro MRI and fluorescence imaging analyses have shown that the PQD@Gd nanoagents are internalized into the cancer cells via a caveolae-mediated endocytosis pathway. The PQD@Gd nanoagents have exhibited excellent biocompatibility even at concentrations as high as 450 ppm. Interestingly, the as-prepared PQD@Gd nanoagents have efficiently produced cytotoxic reactive oxygen species in the cancer cells under 671 nm laser illumination and thereby induced cell death. Moreover, the PQD@Gd nanoagent also demonstrated excellent photocatalytic activity toward organic pollutants under visible light irradiation. The organic pollutants rhodamine b, methyl orange, and methylene blue were degraded by 92.11, 89.21, and 76.21%, respectively, under 60, 80, and 100 min, respectively, irradiation time. The plausible mechanism for the photocatalytic activity is also elucidated. Overall, this work proposes a novel strategy to enhance the optical properties, stability, and bioapplicability of PQDs. The multifunctional PQD@Gd nanoagents developed in this study could be the potential choice of components not only for cancer therapy due to dual-modal imaging and photodynamic therapeutic properties but also for organic pollutant or bacterial removal due to excellent photocatalytic properties.

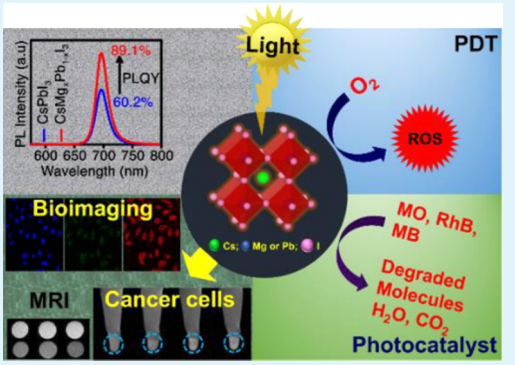

KEYWORDS: *$CsMg_xPb_{1-x}I_3$ QDs, multifunctional nanoagent, reactive oxygen species, MR imaging, and photocatalytic activity*

1. INTRODUCTION

Owing to their exceptional optoelectronic characteristics such as bright display, high absorption coefficient rate, near-unity fluorescence quantum yield (QY), and narrow excitonic bands, perovskite nanocrystals (PNCs) have attracted interest in practical applications including photocatalysis,[1−3] solar cell fabrication,[4,5] white-light-emitting diodes,[6−8] and fluorescent photodetection.[9−12] The three-dimensional perovskite crystal structure (AMX_3) is made up of a corner-shared octahedral unit $[MX_6]^{-4}$, in which the M-site cation [lead (Pb^{2+}), manganese (Mn^{2+}), tin (Sn^{2+})] is coordinated by six X-site anions (Cl^-, Br^-, and I^-) and the A-site cation [cesium (Cs^+), methylamine ($CH_3NH_3^+$, MA), ammonia (NH_3^+)] is embedded in a void surrounded by octahedral unit cells.[13,14] Furthermore, colloidal metal halide nanocrystals have an interesting band arrangement that is defect-tolerant and enables incorporation of atoms or ions into the host structure.[7,14,15] Besides, to adjust the perovskite lattice structure, alleviate crystallographic phases, and achieve diverse optical and electrical properties, the doping strategies that can bring suitable elements into the crowd nanocrystals framework

Received: October 12, 2021
Accepted: December 20, 2021
Published: December 28, 2021

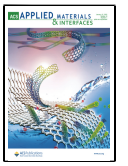

Scheme 1. Schematic Illustration of the Encapsulation of the $CsMg_xPb_{1-x}I_3$ QDs by PF127-Gd Micelle Structure to Produce Water-Soluble a PQD@Gd Nanoagent

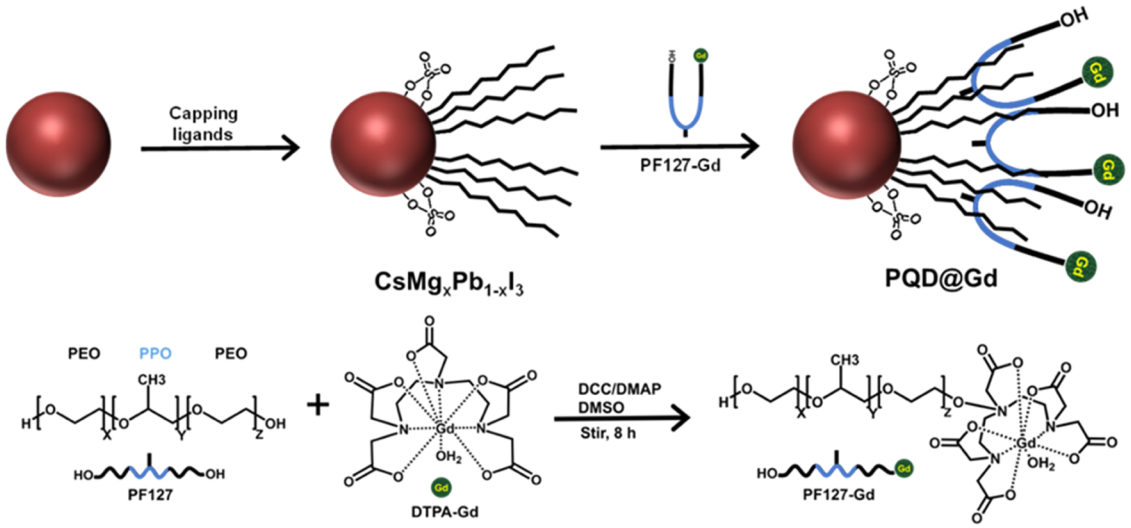

are widely deployed. It has been reported that integrating a M^{2+}-site cation into PNCs could correct the Pb coordination structure and increase the short-range lattice order by correcting the Pb−X octahedral alteration and eliminating surface traps by suppressing halide vacancies, which prevents them from achieving high QY.[16−22] For example, Chen and coworkers[23] recently used Cu^{2+} doping to stabilize orthorhombic-phase $CsPbI_3$. The Cu^{2+}-doped PNCs exhibited not only high formation energy but also high stability than undoped PNCs. Tao et al. produced Sn-doped perovskite ($MA_3Sb_2I_9$) structures using a hydrothermal synthesis approach to construct a high-performance solar cell device. However, this PNC is not frequently employed in photovoltaic applications might be due to the high exciton binding energy and transient oxidation state of Sn ions ($Sn^{2+}\leftrightarrow Sn^{4+}$).[24] Recently, Rakesh et. al reported that Ni^{2+}-integrated $CsPbI_3$ could exhibit intense emission spectra and improved stability. Even though the produced NCs had strong restraint ability and good photovoltaic performance, Ni^{2+} is a Shannon radii cation.[25] These findings suggest the existence of space to propose new divalent cations that can lift the stability and photophysical properties of the red perovskites upon doping. Also, current approaches could help to stabilize the nanocrystals to some extent, but still, there is requirement of robust strategies. Accordingly, herein, we propose that doping with metal ions having comparable ionic radii and stable oxidation states, such as magnesium (Mg), can improve the luminescent quality of freshly produced perovskite quantum dots (PQDs) by simultaneously improving the energy band gap and resolving the Shannon effect.

After successfully employing the hot injection technique by Kovalenko and collaborators,[26] the advancement of adjustable synthetic procedures for obtaining lead halide PNCs takes a big stride forward. This approach consisted of a two-step process that began with the preparation of a Cs-oleate precursor and subsequent injection of the Cs-oleate precursor into a lead-containing flask at high temperatures and under an inert atmosphere. Although the nanocrystals produced owned excellent crystallinity and stability, the intricate arrangement and inert environment posed major drawbacks.[27−30] Microwave irradiation techniques can address the issue of inhomogeneous heating by providing a scalable platform for producing exceptional NCs with improved morphological properties.[31−33]

Despite the fact that PNCs are the most explored material in the production of WLEDs, solar cells, and sensors, they have received less attention in the nanomedicine field because their crystal structure is highly unstable when exposed to air, aqueous conditions, and light irradiation.[27,28,34] As a result, adopting a strategy to improve PNCs' structure stability in polar solvents is particularly desirable, as it will offer a lot of possibilities for using their ultrahigh-resolution imaging in cancer cell diagnostics and combining it with other therapeutic activities. Polymer embedding matrix,[35] inorganic encapsulation,[36] core−shell formation,[37] and chemical transformation[38] are the most commonly employed techniques to convert hydrophobic perovskite QDs into water-soluble QDs. The polymer embedding technique would be more preferable as it can offer a strong hydrophobic protective layer on the PNCs' red wall surface, and similarly, the incorporation of the silica matrix is also critical to achieving stable interaction with water via hydrogen bonding with the alkoxyl group. SiO_2-integrated PQDs, on the other hand, had better morphology and luminescence properties; the silica covering hindered interfacial carrier transfer, which further weakened the performance of PNCs.[1,39] As a result, we were interested in finding an amphiphilic polymer that can simultaneously provide hydrophobic support to the PQD structure while also having a strong tendency to dissolve in water. In this scenario, pluronic (PF127), a triblock copolymer with amphiphilic properties due to poly(ethylene glycol) (a hydrophilic segment) at both ends and poly(propylene glycol) (hydrophobic segment) at the central block, would be an attractive candidate for fabricating water-stable red-emitting QDs. More importantly, because of its amphiphilic nature, PF127 undergoes self-assembly into micelle structures in a wide range of solutions, allowing for loading of drug or other therapeutic agents.[40] Although a recent study demonstrated that water-phase PQD can be used as a bioimaging probe for cancer cell treatment,[4,41] the combination of PQD's fluorescence properties with a theranostic agent has never been reported before. It would be important to combine phototherapeutic and contrast agents in a single platform to pinpoint tumor areas and improve

https://doi.org/10.1021/acsami.1c19644
ACS Appl. Mater. Interfaces 2022, 14, 278−296

cancer therapeutic efficiency. Magnetic resonance imaging (MRI) has shown to be an efficient diagnostic tool due to its higher resolution and tissue penetration than existing fluorescence techniques. PNCs' luminescent features make them ideal for use with MRI contrast agents like Gd imaging modalities. Therefore, PF127 polymer micelles with hydrophilic−hydrophobic segments could be an excellent carrier for incorporating a Gd contrast agent into micelles, as well as PQDs, which could be a viable technique for making dual-modal imaging-guided nanoagents.

In this regard, we have established quick and single-step microwave synthesis of high-quality and controllable morphology red-emitting Mg-doped $CsPbI_3$ QDs for the first time. Thus, the as-prepared $CsMg_xPb_{1-x}I_3$ NCs exhibit superior optical properties with excellent crystallinity and enhanced photostability as compared to the nondoped $CsPbI_3$ NCs. Moreover, the incorporation of Mg^{2+} enhances the tolerance factor, resulting in prolonged stability without affecting the crystalline morphology of the host structure. Herein, for the first time, we demonstrate the fabrication of a water-soluble red-emitting and dual image-guided therapeutic agent (PQD@Gd nanoagent). Gadolinium (Gd), an MRI contrast agent, was combined with PF127 amphiphilic polymer via a DMAP/DCC cross-linker to encapsulate and transfer $CsMg_xPb_{1-x}I_3$ QDs into the aqueous phase, as shown in Scheme 1. Under 671 nm laser irradiation, the PQD@Gd nanoagent produces a significant amount of reactive oxygen species (ROS). Due to the presence of Gd^{3+}, the PQD@Gd nanoagent exhibits a distinct MRI contrasting response. The phototherapeutic effects and MRI response of the PQD@Gd nanoagent have been demonstrated for in vitro cancer cells. Furthermore, the photocatalytic activity of the PQD@Gd nanoagent was also studied for the decomposition of the organic dyes upon visible light treatment. The results suggest that PQD@Gd could be utilized as an efficient nanoagent for MRI-guided photodynamic therapy and outstanding fluorescent imaging capabilities.

2. EXPERIMENTAL SECTION

2.1. Chemicals. Lead chloride ($PbCl_2$, 99%), lead iodide (PbI_2, 99.9%), octadecene (ODE, ≥99.8%), and oleylamine (OAm, 80−90%) were obtained from Acros Organics. Lead bromide ($PbBr_2$, 99.98%) and diethylenetriamine penta-acetic acid (DTPA-Gd, ≥99.9%) were found from Alfa Aesar. Toluene (99.8%, Baker Analyzed) was acquired from J.T. Baker. Cesium acetate (CsAc, 99.99%), magnesium sulfate ($MgSO_4$, 99%), rhodamine B (RhB, 95%), trioctylphosphine oxide (TOP, 90%), 5,5-dimethyl-1-pyrroline *N*-oxide (DMPO, ≥97%), oleic acid (OAc, 65.0-88.0%), 2,2,6,6-tetramethylpiperidine (TEMP, ≥99%), 4′,6-diamidino-2-phenylindole (DAPI, 98%), ascorbic acid (AA, 99.10%), silver nitrate (≥99%), pluronic F127 (PF127), *o*-phenyldiamine (OPD, 98%), isopropanol (IPA, ≥99.5%), methylene blue (MB, ≥82%), methyl orange (MO, 85%), anhydrous ethanol (99.5%), ethylenediamine tetraacetic acid (EDTA, 99%), nitro blue tetrazolium (NBT, 98%), minimum essential medium Eagle (MEME), high-glucose Dulbecco's modified Eagle's medium (DMEM), 2,7-dichlorofluorescin diacetate (DCFH-DA, ≥97%), sodium bicarbonate ($NaHCO_3$, 99.5−100.5%),1,3-dicyclohexyl carbodiimide (DCC, 99%), sodium pyruvate, and 4-dimethylaminopyridine (DMAP, ≥99%) were bought from Sigma-Aldrich. WST-1 (4-[3-(4-Iodophenyl)-2-[4-nitrophenyl]-2H-5-tetrazolio]-1,3-benzene disulfonate) was procured from Roche Applied Science. Hexane (C_6H_{14}) was obtained from UNI-ONWARD (Taiwan). Dimethyl sulfoxide (DMSO) and 1,4-diphenyl-2,3-benzofuran, (DPBF, 99.995%) were purchased from J.T. Baker. All reagents were of analytical grade and were utilized without additional purification.

2.2. Synthesis of $CsPbI_3$ and $CsMg_xPb_{1-x}I_3$ QDs. CsAc (0.1 mmol), 0.3 mmol PbI_2, 0.04 mmol $MgSO_4$, 0.5 mL of OAm, 1 mL of OAc, and 10 mL of ODE were added and mixed for 3 min by ultrasonication (130 W, 60%) to obtain a uniform solution. Then, TOP (2 mL) was added to the resulting solution to aid in the breakdown of the lead precursor, and the mixture was subjected to microwave heating (200 °C for 15 min). Afterward, the resulting solution was cooled to room temperature before being subjected to centrifugation at 6000 rpm for 25 min. The supernatant was removed, and the precipitate was dissolved in 10 mL of hexane and centrifuged again (5000 rpm, 4 min) to remove any bigger particles. The supernatant solution (denoted $CsMg_xPb_{1-x}I_3$) was then collected for further investigation. Except adding a $MgSO_4$ precursor, the same experimental procedure was followed to produce undoped $CsPbI_3$ nanocrystals.

The same experimental technique was employed to fabricate mixed halide perovskite QDs $CsMg_xPb_{1-x}X_3$ (X = Cl, Br, I) by varying the amounts of $PbCl_2$ (0.05, 0.1, 0.2, and 0.3 mmol), $PbBr_2$ (0.05, 0.1, 0.2, and 0.3 mmol), and PbI_2 (0.05, 0.1, 0.2, and 0.3 mmol) precursors with a fixed amount of the CsAc (0.1 mmol) precursor.

2.3. Synthesis of PF127-Gd Carriers. The PF127-Gd conjugates were synthesized by adapting the recently reported protocol.[40] Briefly, PF127 (100 mg in 10 mL) and DTPA-Gd (25 mg/5 mL) were dispersed in DMSO separately. To activate carboxylic groups, DCC (0.05 mmol) and DMAP (0.1 mmol) were added to the DTPA-Gd solution and agitated for 30 min. Subsequently, the activated DTPA-Gd and PF127 solutions were mixed and reacted for 24 h at room temperature. Finally, the PF127-Gd conjugates were purified by dialysis (Mw cut-off: 12 000 Da) against deionized (DI) water for 3 days and lyophilized.

2.4. Encapsulation of $CsMg_xPb_{1-x}I_3$ into PF127-Gd. The $CsMg_xPb_{1-x}I_3$ (10 mg) powder was dispersed in 5 mL of toluene by agitation for 3 min. Next, 0.5 mg of the PF127-Gd powder was added and stirred (500 rpm, 25 min) at a controlled temperature. Finally, the resulting mixed solution was centrifuged (6000 rpm, 15 min) and the obtained precipitate was dried in air. The obtained powder (abbreviated as PQD@Gd nanoagent) was dissolved in a known volume of water.

2.5. Examination of Reactive Oxygen Species (ROS) Generation. The potential of the PQD@Gd nanoagent to generate radical oxygen species under laser irradiation was investigated using a DBPF test, a frequently used reagent for ROS detection. In this, 0.4 mL of the PQD@Gd nanoagent (100 μg/mL) and 20 μL of DPBF (1.5×10^{-3} M) solution were mixed in a quartz cuvette and illuminated under a 671 nm light source at a power density of 2.0 W/cm^2. Then, the PL spectra of DPBF were recorded at an excitation wavelength of 410 nm after every 5 min irradiation for a total of 30 min. The changes in the PL intensity at 460 nm were compared with those before irradiation (0 min).

2.6. Characterization of Generated ROS. Electron spin resonance (ESR) was used to analyze the type of ROS produced by PQD@Gd. The experiment was performed to detect $^1O_2$, $^{\bullet}O_2^-$, and $^{\bullet}$OH ROSby radical trappers 100 mM TEMP (in DMSO) and 100 mM DMPO (with DMSO and H_2O), respectively. In this, 0.9 mL of PQD@Gd solution was mixed with 0.1 mL of spin trapper (either TEMP or DMPO) and then illuminated for 10 min with a 671 nm laser (2.0 W/cm^2) and ESR spectra were recorded.

The generation of $^1O_2$ was further confirmed by analyzing the PL spectra at 1270 nm that were recorded after irradiation. The mixture was treated using a 671 nm light source at a power density of 2.0 W/cm^2 after saturating 3 mL of PQD@Gd (100 μg/mL in D_2O) with oxygen gas for 10 min. The fluorescence spectra were monitored at around 1270 nm ($\lambda_{excitation}$ = 671 nm).

The generation of $^{\bullet}O_2^-$ radical was examined by the NBT assay following the reported protocol. About 200 μL of 100 mM NBT was mixed with 400 μL of PQD@Gd (100 μg/mL) in a quartz cuvette and treated with a 671 nm light source (2.0 W/cm^2) for 5 min. The

https://doi.org/10.1021/acsami.1c19644
ACS Appl. Mater. Interfaces 2022, 14, 278−296

absorbance of the solution following laser irradiation was monitored at 260 nm.

The generation of •OH radical was investigated using the OPD solution. The •OH radical oxidizes OPD to yellowish 2,3-diaminophenazine (DAP), which exhibits absorbance at 450 nm. Thus, 100 μL of OPD (10 mM in DI water) was sonicated with 400 μL of PQD@Gd (100 μg/mL) and illuminated for 5 min with a 671 nm laser (2.0 W/cm^2). Then, ultraviolet−visible (UV−vis) absorption spectrometry was employed to measure the absorption spectra of oxidized OPD at 450 nm.

2.7. Photocatalytic Activity of the PQD@Gd Nanoagent. The photocatalytic performance of the PQD@Gd nanoagent was examined using the degradation of organic pollutants rhodamine B (RhB), methyl orange (MO), and methylene blue (MB) under visible lamp irradiation. To attain adsorption−desorption reaction equilibrium between the catalyst and the MO solution, 1 mg/mL PQD@Gd nanoagent powder was dissolved in 20 mL of MO solution (1 mM in ethanol) and the suspension was stirred for 10 min in the dark. The suspension was then illuminated under 671 nm visible light at a distance of 5 cm between the light source and the suspension liquid and centrifuged for 10 min at 5000 rpm to remove the photocatalyst nanoparticles. The degradation of MO was detected using UV−vis spectroscopy at 460 nm. The same experimental procedure was followed for the degradation study of 1 mM MB and 1 mM RhB. The absorption spectra of MB and RhB at 664 and 550 nm, respectively, were monitored every 10 min to determine their degradation. The degradation efficiency was calculated as follows

$$\text{degradation efficiency} = \frac{(A_o - A)}{A_o} \times 100\%$$

where A_o and A denote the initial concentration and the concentration after the time of irradiation, respectively. The reusability of the PQD@Gd nanoagent was tested toward MO, RhB, and MB organic dyes.

2.8. Detection of Active Species. To identify the role of various types of photocatalytic-dependent radicals and reaction pathways, a series of trapping tests were accomplished. Prior to the addition of the PQD@Gd photocatalyst, silver nitrate ($AgNO_3$), ascorbic acid (AA), isopropyl alcohol (IPA), ethylenediamine tetraacetic acid (EDTA), and β-carotene were used as radical trappers for holes (h^+), superoxide radicals ($^•O_2^-$), hydroxyl radicals (•OH), electrons (e^-), and singlet oxygen ($^1O_2$), respectively. The mixture was exposed to a 671 nm light source at a power source of 2.0 W/cm^2 and then centrifuged to remove photocatalyst nanoparticles. UV−vis spectroscopy was utilized to determine the concentration of the supernatant solution. The photodegradation was estimated and compared to a control experiment in which no radical trapping reagent was utilized.

2.9. Evaluation of In Vitro Biocompatibility of the PQD@Gd Nanoagent. The WST-1 test was employed to examine in vitro cell viability. The biocompatibility investigations were performed on human liver carcinoma (HepG2) cells, mouse melanoma (B16F1), and human cervical cancer (HeLa) cells. First, the cells were cultured to confluence at 37 °C and 5% CO_2 in EMEM (for HeLa) or DMEM (for B16F10 and HepG2) medium containing 1% antibiotic−antimycotic, 1% nonessential amino acids, 1% L-glutamine, 1% sodium pyruvate, and 10% FBS.

After that, the cells were washed and harvested from culture plates. About 1 × 10^4 cells/well were placed in each 96-well flat-bottomed plate and cultured for 24 h. Then, 100 μL of fresh medium was supplied along with various concentrations of the PQD@Gd nanoagent (0, 100, 200, 300, 400, and 450 μg/mL) and kept for predetermined time points (24, 48, and 72 h). At each time point, 10 μL of WST-1 reagent was added to each well and kept for 2 h. To quantify cellular viability, the absorbance at 450 nm was determined using a model 680 XR microplate reader (Bio-Rad). By equating the absorbance value of treated cells with that of the control experiment (untreated cells), the relative cell viability (%) was computed. For every test, the experiment was performed three times.

2.10. Evaluation of PDT-Mediated Cell Toxicity. In this experiment, cancer cells were cultured in a 96-well plate at 1.0 × 10^4 per well for 24 h at 37 °C and 5% CO_2. After that, the old medium was washed with phosphate-buffered saline (PBS), and 100 μL of fresh cell medium having various concentrations of PQD@Gd was added to each well followed by incubation for 6 h for cell internalization. Then, the cells were treated with a 671 nm light source (power density of 2.0 W/cm^2) for 5 min. The irradiated cells were incubated for another 24 h, and the cell viability was determined by the WST-1 assay.

2.11. Analysis of In Vitro MR Imaging. To explore the contrasting effect of the as-prepared PQD@Gd nanoagent, the concentration of Gd^{3+} ions was assessed by inductively coupled plasma atomic emission spectroscopy (ICP-AES). Cancer cells were seeded for 1 day in a 50 mL serum bottle with 5 mL of medium added. The old medium was then removed and rinsed using PBS, and fresh medium containing the PQD@Gd nanoagent at various concentrations was added. Cells were then trypsinized, rinsed, and resuspended in PBS after a 24 h incubation period. A Bruker MedSpec 7T MRI machine with a birdcage head coil was utilized to acquire MR pictures of cells inside 0.2 mL tubes.

2.12. Examination of Intracellular Imaging. HepG2, B16F1, and HeLa cells were cultured for 24 h on glass slides assembled in a six-well glass plate containing 2 mL of culture medium. After that, the cells were rinsed twice with PBS, fresh cell medium comprising the PQD@Gd nanoagent at varying concentrations was added to the wells, and the plate was placed in an incubator for 6 h. The cells were harvested by removing the cell medium along with the non-internalized material. Then, the cell nuclei were marked with DAPI based on the manufacturer's instructions after treatment with 2 mL of ethanol (75% purity). Finally, confocal laser scanning microscopy (CLSM, Leica, Germany) was employed to capture the fluorescence pictures of the cells.

2.13. Endocytosis Trafficking Assay. HeLa cells were cultured on glass slides that were fixed in a six-well plate. Next, the cells were pretreated with a culture medium diluted with various inhibitors including amiloride hydrochloride (2.5 mM), nystatin (50 μg/mL), genistein (100 μg/mL), and MβCD (16 mM) for 1 h. Following this, the medium was withdrawn and fresh medium containing the PQD@Gd nanoagent was added and incubated for 3 h. Then, the cells were cultured with DAPI (blue) reagent for 20 min to mark the nucleus structure. In the end, confocal microscopy was used to track nanoagent internalization.

By varying the incubation temperature, an energy-dependent mechanism of cellular ingestion was demonstrated. HeLa cells were cultivated as mentioned above and supplied with nanoagents at various temperatures such as 4 and 37 °C. The glass slides were made as previously described, and the images were obtained using confocal microscopy.

2.14. Intracellular ROS Detection. HeLa cells were grown for 1 day as indicated in Section 2.12. After that, fresh medium containing the PQD@Gd nanoagent at various concentrations was supplied to the cells followed by incubation for 6 h. The medium was then removed from each well, and the wells were rinsed twice with PBS to eliminate any non-ingested material. Then, the cells were incubated with 10 μL of DCFH-DA for 2 h and exposed to 671 nm light (2.0 W/cm^2) for 5 min. Finally, the cell images were recorded using confocal microscopy.

2.15. Characterization Techniques. Optical characterization of the as-prepared material was performed by ultraviolet−visible absorption spectrometry (UV−vis; model FP-6500, Jasco Co. Ltd.), photoluminescence spectrometry (PL; model Fluorolog-3, Horiba Jobin Yvon), and time-resolved photoluminescence (TRPL; model NanoHarp, Pico Quantity). The morphological study was carried out by transmission electron microscopy (TEM; model Tecnai F20 G2 FETEM, Philips; model JEM-2100F, JEOL). X-ray photoelectron spectroscopy (XPS) was conducted using an ESCALAB 250 (VG Scientific). X-ray diffraction (XRD) was performed using a Bruker D8 Discover diffractometer equipped with monochromatized Cu Kα radiation (wavelength 1.54 Å). Fourier transform infrared (FTIR)

https://doi.org/10.1021/acsami.1c19644
ACS Appl. Mater. Interfaces 2022, 14, 278−296

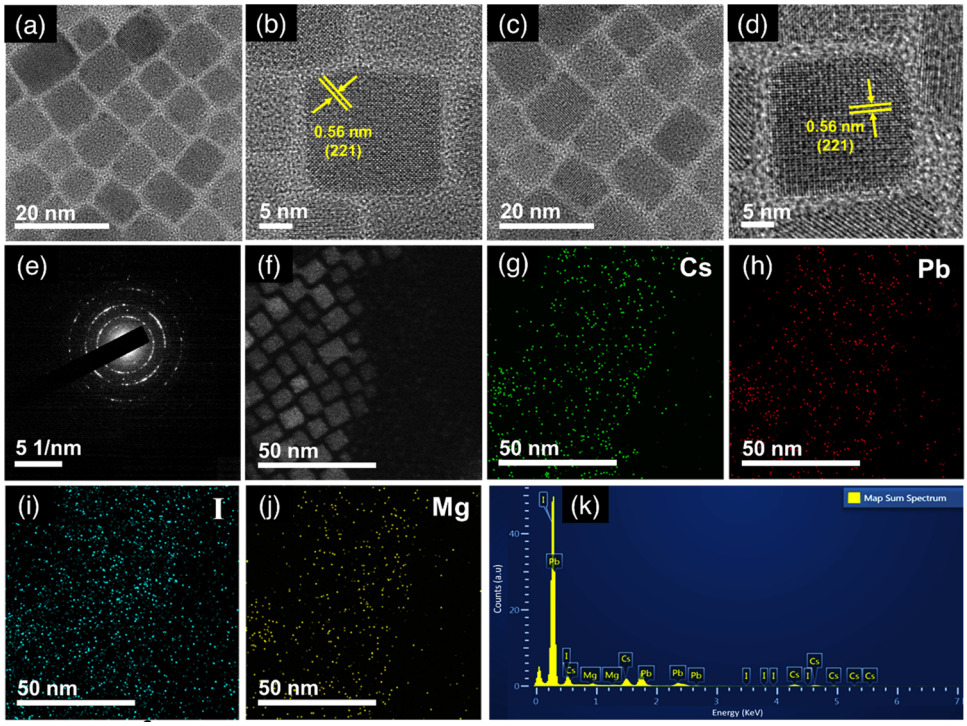

Figure 1. TEM images of (a) $CsPbI_3$ and (b) $CsMg_xPb_{1-x}I_3$ QDs. HRTEM images of (c) $CsPbI_3$ and (d) $CsMg_xPb_{1-x}I_3$ QDs. (e) SAED image of $CsMg_xPb_{1-x}I_3$ QDs. (f) HAADF-scanning transmission electron microscopy (STEM) image and elemental mapping images of (g) Cs, (h) Pb, (i) I, and (j) Mg for $CsMg_xPb_{1-x}I_3$ QDs. (k) EDS spectrum for $CsMg_xPb_{1-x}I_3$ QDs.

spectrometry was performed using an FTS-3500 (Bio-Rad). Ultraviolet photoelectron spectrometry (UPS) (ESCALab250Xi, Thermo Scientific) was used to estimate the valence band (VB) of QDs. A Zetasizer 2000 (MALVERN) was utilized to examine the ζ-potential. The average size of the nanomaterials was computed by dynamic light scattering (DLS) (model Nano-ZS90, Malvern). The viable cell measurement was performed by employing an ELISA reader (model Power Wave XS, BioTek). Inductively coupled plasma atomic emission spectroscopy (ICP-AES; Horiba JY2000-2) was utilized to calculate the amount of Gd in PQD@Gd nanocomposites. Electron spin resonance (EPR) spectra were acquired at 10 K using a Bruker Elexsys E-580 spectrometer (Bruker, Germany). Magnetic resonance imaging (MRI) was performed on a Bruker MedSpec 7T whole-body system (Ettlingen, Germany) with a birdcage head coil. Confocal laser scanning microscopy (CLSM) under a TCS SP2 device (Leica, Germany) was employed to capture the fluorescence and cellular images. Rhodamine B dye (QY = 68.9% in 95% ethanol) was used as the standard reference to calculate the QY of red-emitting QDs, $QY_{NCs} = QY_{ref} \times \frac{a_{ref}}{a_{NCs}} \times \frac{A_{NCs}}{A_{ref}} \times \left(\frac{n_{NCs}}{n_{ref}}\right)^2$, where the notions NCs and ref represent the as-prepared perovskite material and standard reference dye, respectively, a is the absorbance adjusted in between 0.05 and 0.059, and A refers to the integrated area of the PL intensity for both NCs and the reference dye.

3. RESULTS AND DISCUSSION

3.1. Preparation and Characterization of $CsPbI_3$ and $CsMg_xPb_{1-x}I_3$ QDs. The highly luminescent red-emitting $CsMg_xPb_{1-x}I_3$ NCs were synthesized using the microwave heating technique, as shown in Figure S1. In a standard experiment, CsAc, PbI_2, $MgSO_4$ (source of the Mg dopant), and a capping ligand as the stabilizer were mixed appropriately and subjected to optimized reaction conditions (200 °C, 15 min). The amount of Mg in $CsMg_xPb_{1-x}I_3$ NCs was varied using different molar ratios of $MgSO_4$. The undoped $CsPbI_3$ NCs were synthesized using the same procedure by avoiding the use of $MgSO_4$.

The structural morphology of the as-synthesized $CsPbI_3$ and $CsMg_xPb_{1-x}I_3$ QDs was determined using X-ray diffraction (XRD) and transmission electron microscopy (HRTEM). The TEM images of $CsPbI_3$ (Figure 1a) and $CsMg_xPb_{1-x}I_3$ (Figure 1b) indicated that both the fabricated NCs had the same cubelike morphology and well-oriented lattice fringes with estimated sizes of 14 and 15 nm, respectively. The cubic geometry of the NCs remained unchanged even after doping with Mg^{2+} ions. The DLS test was employed to estimate the size distribution of $CsPbI_3$ and $CsMg_xPb_{1-x}I_3$ QDs, and the obtained results validated that both $CsPbI_3$ and $CsMg_xPb_{1-x}I_3$ NCs had average sizes of 14.79 and 15.62 nm, respectively (Figure S2a,b). The HRTEM image of $CsMg_xPb_{1-x}I_3$ QDs (Figure 1d) showed that the interplanar distance of the (221) lattice plane was 0.56 nm and well matched with the crystalline plane of pristine $CsPbI_3$ NCs (Figure 1c). However, the interplanar distance was 0.55 nm (Figure S2c) for 0.08 mmol Mg^{2+}-doped $CsPbI_3$ QDs. The representative selected area electron diffraction (SAED) pattern for $CsMg_xPb_{1-x}I_3$ QDs shown in Figure 1e illustrated that the perovskite structure possessed a high degree of crystallinity. Using elemental mapping and energy-dispersive X-ray spectroscopy (EDS) techniques, the integration and distribution of compositional ions, including the guest cation (Mg^{2+}), were demonstrated. We noticed that the EDS scans were carried out in regions with a high number of NCs in an attempt to gather clinically significant information. Figure 1f depicts a magnified high-angle annular dark-field (HAADF) image showing that $CsMg_xPb_{1-x}I_3$ QDs owned cubic morphology. Figure 1g–j displays the elemental mapping results, which reveal that each individual ion, such as Cs, Pb, I, and Mg, is evenly distributed across the lattice structure. Furthermore, no phase segregation

https://doi.org/10.1021/acsami.1c19644
ACS Appl. Mater. Interfaces 2022, 14, 278−296

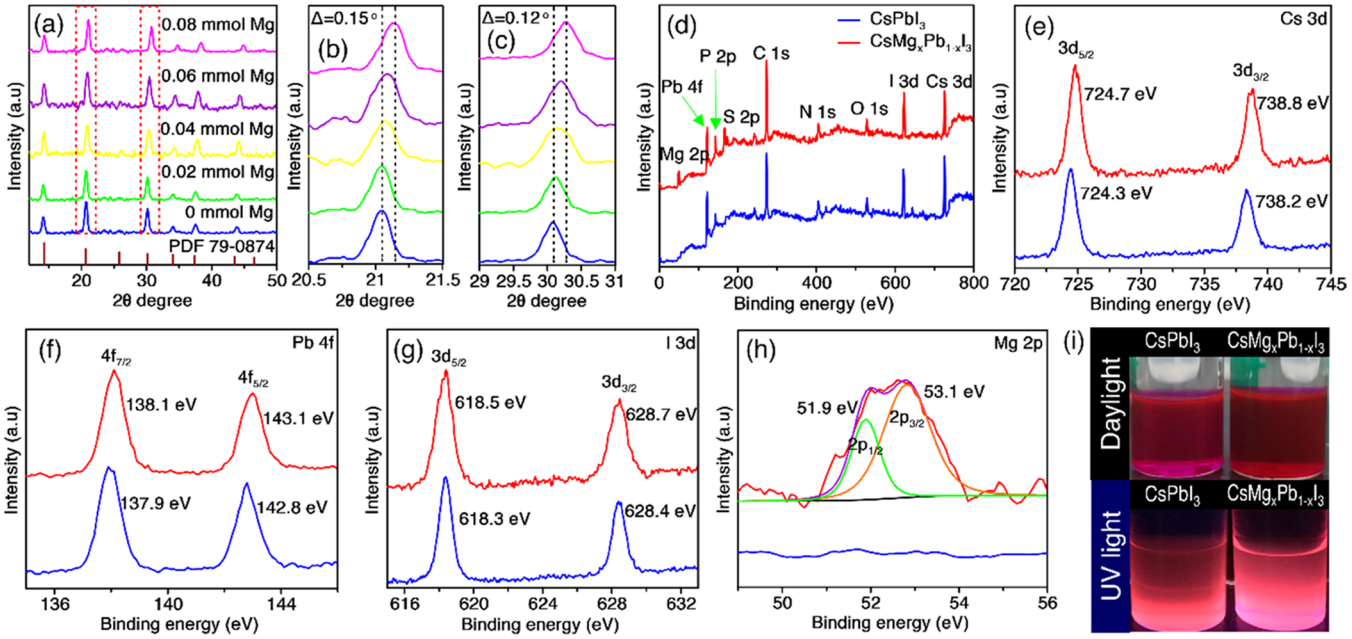

Figure 2. (a) XRD pattern of $CsPbI_3$ QDs doped with different molar ratiod (0, 0.02, 0.04, 0.06, and 0.08 mmol) of Mg^{2+} ions. Magnified view of the (b) 220 and (c) 221 XRD peaks with a systematic shift in the peak position with increasing Mg dopant concentration. XPS spectra of $CsPbI_3$ and $CsMg_xPb_{1-x}I_3$ QDs: (d) survey spectra of $CsPbI_3$ and $CsMg_xPb_{1-x}I_3$ QDs and high-resolution XPS spectra for (e) Cs 3d, (f) Pb 4f, (g) I 3d, and (h) Mg 2p of $CsPbI_3$ and $CsMg_xPb_{1-x}I_3$ QDs. (i) Photographic images of $CsPbI_3$ (left) and $CsMg_xPb_{1-x}I_3$ (right) QDs taken at daylight and under a UV lamp, respectively.

or surface preference were identified, suggesting that the Mg^{2+} ion distribution was uniform. Inductively coupled plasma atomic emission spectroscopy (ICP-AES) measurements were performed to further validate the practical concentration of Mg^{2+} in $CsMg_xPb_{1-x}I_3$ QDs. It was observed that 0.011, 0.032, 0.051, and 0.069% Mg^{2+} ions were present in $CsMg_xPb_{1-x}I_3$ QDs synthesized using 0.02, 0.04, 0.06, and 0.08 mmol $MgSO_4$, respectively (Table S1), suggesting that a substantial quantity of Mg^{2+} ion was integrated into the QD structure. These results are completely in agreement with the data obtained using EDS mapping.

The XRD peaks of $CsPbI_3$ and $CsMg_xPb_{1-x}I_3$ QDs shown in Figure 2a were in line with those of standard data (JCPDS#79-0874), and they were mismatched to each other due to Mg doping. The diffraction pattern demonstrated that $CsMg_xPb_{1-x}I_3$ with the Pm3m space group was highly crystalline and adopted a cubic phase. Moreover, different strong peaks were observed at θ; 15.38, 21.67, 31.6, 34.58, 36.9, and 44.3°, which could be well oriented to 110, 220, 211, 310, 221, and 112 crystal faces of the cubic perovskite phase, respectively. In the XRD scans, no additional impurity peaks or new phases attributed to Mg ions were observed, suggesting that doping with Mg ions did not alter the crystal arrangement of pristine $CsPbI_3$. However, further analysis of peaks of 220 and 211 planes (Figure 2b,c) revealed that doping with Mg^{2+} ions caused peak shifts, which became larger as the concentration of Mg^{2+} increased. The shift in peak positions could be credited to lattice shrinkage caused by the exchange of larger Pb ions (r_{Pb} = 0.133 nm) with smaller Mg^{2+} ions (r_{Mg} = 0.087 nm). Precisely, as the Mg^{2+} concentration increased from 0 to 0.08 mmol, the diffraction peaks drifted toward a higher angle, implying that smaller Mg^{2+} cations replaced Pb^{2+} cations in octahedral positions and resulted in progressive lattice contraction. The shifting panel of the (220) and (221) peaks in Figure 3b,c indicated that Mg^{2+} enters the host by occupying lead lattice sites in the perovskite crystal structure. Moreover, the tolerance factor (TF) was computed using the following equation[21]

$$TF = \frac{r_A + r_X}{\sqrt{2}(r_B + r_X)}$$

The TF value of $CsMg_xPb_{1-x}I_3$ NCs was deduced as 0.93, which is better than that of undoped $CsPbI_3$ (0.80), suggesting that doping with smaller-sized metal ions such as Mg^{2+} could enhance the phase stability of $CsMg_xPb_{1-x}I_3$ over $CsPbI_3$ QDs.[42,43]

The distribution of ions in $CsPbI_3$ and $CsMg_xPb_{1-x}I_3$ QDs was investigated by employing X-ray photoelectron spectroscopy (XPS). As displayed in Figure 2d, the complete XPS scan spectra of both $CsPbI_3$ and $CsMg_xPb_{1-x}I_3$ exhibited peaks corresponding to Cs 3d, Pb 4f, and I 3d at around 725, 138, and 628 eV, respectively. A new peak at around 53 eV corresponding to Mg 2p was observed in $CsMg_xPb_{1-x}I_3$ spectra, confirming the doping of Mg ions into the host lattice. Because of capping ligands, additional signal peaks relating to N 1s, O 1s, C 1s, S 2p, and P 2p were observed in the XPS spectra. The peaks of Cs 3d, Pb 4f, and I 3d orbitals in QD samples were close-fitting with identical dominating peaks, signifying that Mg^{2+} doping does not affect the local binding environment. The changes in the binding energies were analyzed using high-resolution XPS (HRXPS). The Cs 3d peak of $CsPbI_3$ NCs deconvoluted into two peaks at binding energies of 738.2 and 724.3 eV, which could be ascribed to $3d_{3/2}$ and $3d_{5/2}$ signals, respectively; however, the binding energies of these signals in $CsMg_xPb_{1-x}I_3$ QDs positively shifted by 0.4 and 0.6 eV, respectively (Figure 2e). The Pb 4f peak of $CsPbI_3$ NCs exhibited two integrated peaks for $4f_{5/2}$ and $4f_{7/2}$ at B.E. values of 142.8 and 137.9 eV, respectively (Figure 2f); however, the binding energies of Pb $4f_{7/2}$ and $4f_{5/2}$ in $CsMg_xPb_{1-x}I_3$ QDs shifted to 143.1 and 138.1 eV,

https://doi.org/10.1021/acsami.1c19644
ACS Appl. Mater. Interfaces 2022, 14, 278−296

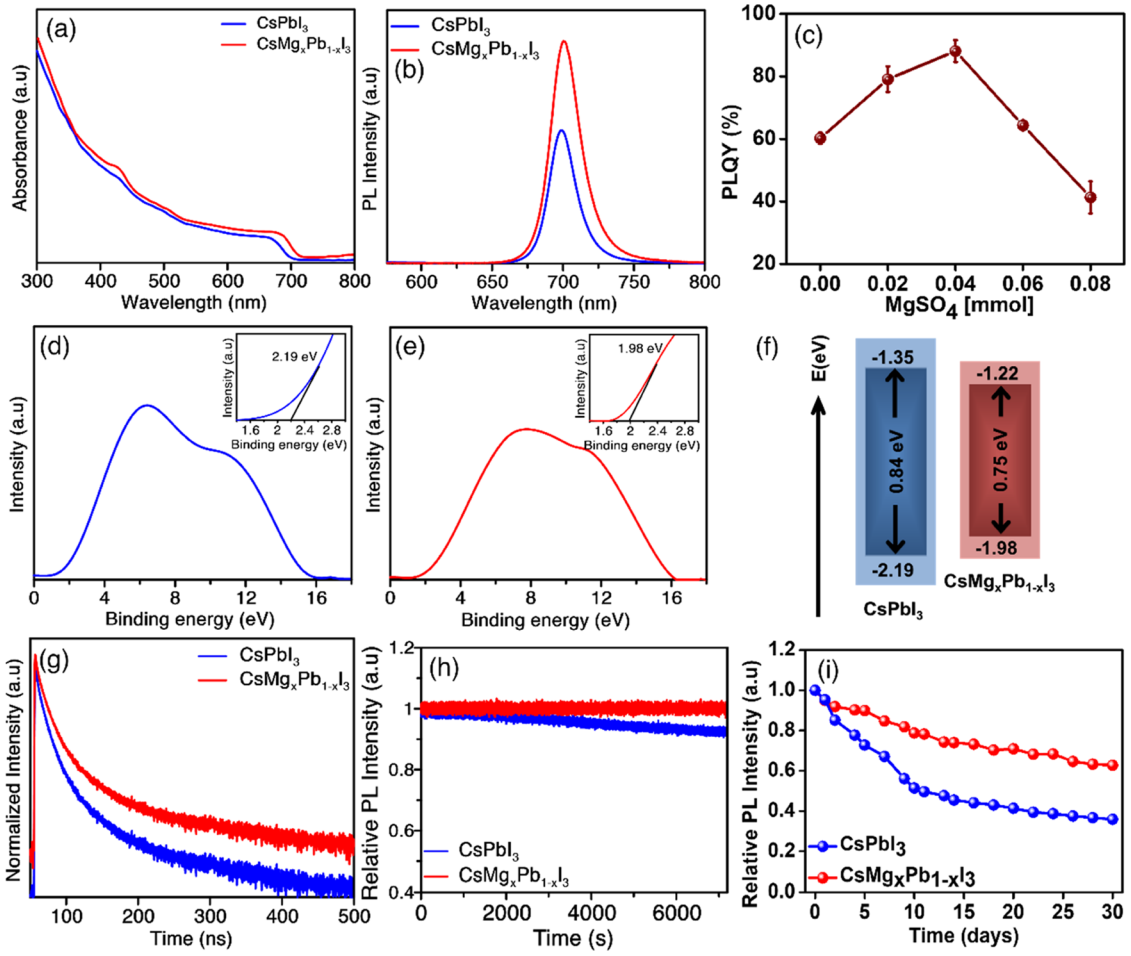

Figure 3. (a) Absorption spectra of $CsPbI_3$ and $CsMg_xPb_{1-x}I_3$ QDs. (b) PL intensity of $CsPbI_3$ and $CsMg_xPb_{1-x}I_3$ QDs measured using an excitation wavelength ($\lambda_{excitation}$) of 370 nm. (c) PLQY variation properties of $CsMg_xPb_{1-x}I_3$ QDs versus different molar ratios of the $MgSO_4$ precursor. UPS spectroscopic analysis for (d) $CsPbI_3$ and (e) $CsMg_xPb_{1-x}I_3$ QDs. (f) Schematic diagram of the band gap energy level diagrams for $CsPbI_3$ and $CsMg_xPb_{1-x}I_3$ QDs. (g) Time-resolved PL decays for excitonic luminescence of $CsPbI_3$ and $CsMg_xPb_{1-x}I_3$ QDs. (h) Photostability performance of $CsPbI_3$ and $CsMg_xPb_{1-x}I_3$ QDs after continuous excitation at 370 nm wavelength. (i) Relative PL intensity properties for $CsPbI_3$ and $CsMg_xPb_{1-x}I_3$ NCs measured at different storage days.

respectively. These outcomes implied that the addition of Mg^{+2} to the lattice could prevent the formation of l vacancies in $CsPbI_3$ NCs and influence the electron density surrounding the host cations of Cs 3d and Pb 4f. The deconvoluted XPS spectra of I 3d in $CsPbI_3$ QDs demonstrated two peaks at 628.4 and 618.3 eV, corresponding to $3d_{5/2}$ and $3d_{3/2}$ signals, respectively, as shown in Figure 2g; nevertheless, in $CsMg_xPb_{1-x}I_3$ NCs, these peaks shifted positively by 0.2 eV for $3d_{5/2}$ and 0.3 for $3d_{3/2}$ eV, which could be because of the formation of Mg−I cross bonds in the octahedral position. After doping with Mg^{2+} ions into host $CsPbI_3$ NCs, the positive shift in the B.E. of Cs ($3d_{5/2}$ and $3d_{3/2}$), Pb ($4f_{7/2}$ and $4f_{5/2}$), and I ($3d_{5/2}$ and $3d_{3/2}$) suggested the existence of a halide-rich chemical environment around the $[PbI_6]^{4-}$ octahedra. The HRXPS of Mg showed two distinct peaks at B.E. values of 51.52 and 53.89 eV (Figure 2e), which could be ascribed to the $2p_{1/2}$ and $2p_{3/2}$ peaks of core Mg^{2+}, respectively, validating the integration of Mg^{+2} ions into the host NCs. These observations further verified that the Mg^{2+} ions integrated into the $CsPbI_3$ perovskite matrix replaced the Pb^{2+} sites, that the Mg^{2+} ions had a greater binding affinity with I^- than Pb^{2+}, and that the interactions between extranuclear and core electrons in both these neighboring ions (Pb^{2+} and I^-) were partially hindered due to Mg's lower electronegativity than Pb. Similar trends were identified in Ni-doped $CsPbCl_xBr_{3-x}$ and Cd-integrated $CsPbCl_3$ NCs.[44,45] The obtained XPS and XRD results, which are in good agreement with each other, indicated the partial substitution of Pb^{2+} octahedral ions in PbI_6 by Mg^{2+} in the $CsMg_xPb_{1-x}I_3$ QDs and increased phase stability and uniformity of the PNCs upon doping with Mg.

3.2. Photophysical Properties of $CsMg_xPb_{1-x}I_3$. The photophysical characterizations of $CsPbI_3$ and $CsMg_xPb_{1-x}I_3$ QDs were monitored using UV−vis absorption and fluorescence spectroscopy techniques. The as-prepared resulting NCs dispersed in hexane emitted dark red luminescent light in daylight and bright red light under UV irradiation, as shown in Figure 2h. The UV−vis absorption spectra of $CsMg_xPb_{1-x}I_3$ NCs demonstrated a slight variation in the first excitonic peak located at 683 nm and the absorption band compared to those of $CsPbI_3$ NCs (Figure 3a), revealing that Mg^{2+}-doped QDs were slightly larger in size. The absence of subsequent structural alteration after successful integration of the Mg^{2+} ions was could be noted by the presence of a weak band edge (Urbach tail), which further implies that both pristine and Mg-doped samples had superior crystallinity with

https://doi.org/10.1021/acsami.1c19644
ACS Appl. Mater. Interfaces 2022, 14, 278−296

a sharp absorption peak and no substantial variations in spectral shapes. Figure 3b depicts the emission spectra of $CsPbI_3$ and $CsMg_xPb_{1-x}I_3$ QDs measured at an excitation wavelength ($\lambda_{excitation}$) of 370 nm. It was observed that $CsMg_xPb_{1-x}I_3$ QDs exhibited a significantly higher PL intensity than pristine $CsPbI_3$ QDs under similar conditions, with very minor red shifts from 699 to 702 nm. The narrow peak spectra of the QDs suggested that QDs with uniform sizes were synthesized. Moreover, the full width at half-maximum (FWHM) of 0.04 mmol Mg-doped QDs was measured to be 38 nm, which is slightly higher than that of undoped QDs (36.2 nm). The increase in FWHM and the slight shift in absorption spectra could be ascribed to the increased size of QDs upon doping with Mg^{2+}, which is in good agreement with recent reports on Zn^{2+}- or Ni^{2+}-doped $CsPbI_3$ NCs.[21,46] Additionally, the PLQY of resulting Mg-doped QDs was plotted against the $MgSO_4$ feeding ratio (Figure 3c), showing that the PLQY increased progressively from 60.2% (undoped QDs) to 89.1% for 0.04 mmol Mg-doped QDs and then decreased to 44.6% for 0.08 mmol Mg-doped QDs. Henceforth, $CsMg_xPb_{1-x}I_3$ QDs means $CsPbI_3$ NCs doped with 0.04 mmol $MgSO_4$. To further confirm the minor variation in the absorption spectra of $CsPbI_3$ and $CsMg_xPb_{1-x}I_3$ QDs, we used UPS to analyze their band gap difference. Thus, the valence band maxima for undoped and Mg-doped QDs were observed at 2.19 and 1.98 eV, respectively. The optical band gap energies of $CsPbI_3$ and $CsMg_xPb_{1-x}I_3$ QDs were computed by extrapolating linear regions from $(\alpha h\nu)^2$ plots against photon energy ($h\nu$), as shown in Figure S3. By integrating the optical band gap energies, the conduction band minima of $CsPbI_3$ and $CsMg_xPb_{1-x}I_3$ QDs were calculated to be 1.35 and 1.22 eV, respectively. These experimental results confirmed that Mg^{2+} cations were successfully doped into the $CsPbI_3$ framework structure.

To acquire a better understanding of the remarkable improvement in PLQY and radiative recombination rate of Mg^{2+}-doped $CsPbI_3$ QDs, time-resolved PL (TRPL) lifetime measurements were performed using TCSPC techniques. The time-resolved PL decay lifetimes of pristine and Mg^{2+}-doped $CsPbI_3$ NCs were studied at an excitation wavelength of 378 nm. The biexponential decay function equation $I(t) = A_1e^{-t/\tau_1} + A_2e^{-t/\tau_2}$ was used to fit the PL decay curves, where $I(t)$ refer to the PL function of time (t) and A_1 and A_2 represent the amplitudes of shorter τ_1 and longer τ_2 lifetimes, respectively. The average PL lifetime (τ_{ave}) was estimated from A_i and τ_i values by the following equation: $\tau_{ave} = \frac{(A_1\tau_1^2 + A_2\tau_2^2)}{(A_1\tau_1 + A_2\tau_2)}$. Table S2 provides the appropriate fitting parameters and their respective amplitudes. The average decay lifetime of $CsPbI_3$ QDs was computed to be 30.43 ns, with τ_1 and τ_2 of 11.55 and 49.68 ns, respectively, whereas the $CsMg_xPb_{1-x}I_3$ QDs exhibited an average PL lifetime of 51.89 ns, with a τ_1 of 17.24 ns and a τ_2 of 86.54 ns. The PL decay lifetime of $CsPbI_3$ NCs increased to 51.78 from 30.12 ns after doping with Mg^{2+}, suggesting that Mg doping can promote exciton recombination via the radiative pathway while suppressing nonradiative decay and surface recombination, thereby improving the PLQY of $CsMg_xPb_{1-x}I_3$ QDs by up to ~89%. From this, the plausible explanation of the effect of Mg concentration on PLQY was deduced as follows: (1) doping a small concentration of Mg into the $CsPbI_3$ host lattice could lift the order in the local chemical binding of lead and promote short-range ordering without making a new recombination channel that would encourage radiative recombination by reducing surface trap states, thereby leading to an enhancement in PLQY. (2) However, an excess amount of Mg^{2+} ions could produce more surface trap states, which causes a reduction in the average lifetime and radiative decay rate of QDs and thereby decreases the PLQY of resulting $CsMg_xPb_{1-x}I_3$. Additionally, the presence of H_2O molecules and SO_4^{2-} ions in the Mg precursor is responsible for ionic instability and aggregation of PNC structures, respectively, resulting in low PLQY.

Next, the stability of the $CsPbI_3$ and $CsMg_xPb_{1-x}I_3$ NCs to light and moisture was investigated. Figure 3h shows the relative PL stability of the as-prepared perovskite QDs under continuous UV lamp irradiation at an excitation wavelength of 370 nm. After 2 h of continuous UV lamp irradiation, the PL intensity of the $CsPbI_3$ QDs decreased by 9.5%, whereas that of the $CsMg_xPb_{1-x}I_3$ QDs remained unchanged, indicating that $CsMg_xPb_{1-x}I_3$ had greater photostability than the undoped QDs. The effect of moisture on the stability of QDs was examined by measuring the PL intensity of QDs after one month of storage. Figure 3i depicts that $CsPbI_3$ and $CsMg_xPb_{1-x}I_3$ QDs retained 40 and 70%, respectively, of their initial PL intensities, suggesting that $CsMg_xPb_{1-x}I_3$ QDs had more storage stability than $CsPbI_3$ QDs. The sulfate ions present on the surface of $CsMg_xPb_{1-x}I_3$ QDs could create steric hindrance and protect QDs from air or moisture, empowering long-term stability.

To investigate the underlying mechanism for the enhanced optical properties of $CsMg_xPb_{1-x}I_3$ NCs, various control experiments were conducted. Upon confirming that Mg^{+2} could increase the PL intensity, the effect of Mg^{+2} concentrations on PL intensity was examined by varying the feeding ratio of the Mg precursor from 0 to 0.08 mmol. As shown in Figure S4a, the PL intensity of resulting Mg-doped NCs increased as the feeding ratio of $MgSO_4$ increased from 0 to 0.04 mmol; however, it diminished upon a further increase in the $MgSO_4$ feeding ratio. The dopant precursor $MgSO_4 \cdot 2H_2O$ comprised Mg^{2+} ions, SO_4^{2-} ions, and 2 moles of water molecules, so further investigation was carried out to study the effect of each ion/molecule on the PLQY of $CsMg_xPb_{1-x}I_3$ NCs. In the literature reports, it has been mentioned that a small amount of the cation dopant or additive can significantly improve the optical properties of QDs as well as their morphological structures. For instance, recent studies have found that M-site-doped perovskite structures (substitution of Pb^{2+} ions), such as Bi-doped $CsPbI_3$ and Ni-doped $Cs_xPb_{1-x}I_3$, resulted in an increased PLQY of perovskite QDs due to the elimination of the surface trap state and increased radiative decay rate.[21,46,47] MgI_2 was used in place of $MgSO_4 \cdot 2H_2O$ as the Mg precursor to figure out the effect of Mg^{+2} ions on PLQY. The PLQY of resulting $CsMg_xPb_{1-x}I_3$ QDs increased to 73.4% for 0.1 mmol MgI_2 and then decreased upon a further increase in MgI_2 (Figure S4b), indicating that Mg^{2+} ions are crucial for PL enhancement of $CsMg_xPb_{1-x}I_3$ NCs. Similarly, sulfobetaine and phosphocholine were used as zwitterionic capping ligands in the fabrication of $CsPbBr_3$ QDs, resulting in enhanced chemical stability and high quantum yield (90%).[48] In another report, a combination of an anionic ligand and $PbBr_2$ reduces the surface traps, stabilizing the PbX_6 octahedral structure and restoring the high QY performance.[15] Subsequently, 10 μL of H_2SO_4 was employed as the additive in the synthesis of PNCs to mimic the SO_4^{2-} ions of $MgSO_4$. The PLQY of resulting $CsPbI_3$ NCs (68.9%) was higher than that of pristine $CsPbI_3$ NCs (60.2%) (Figure S4c). These outcomes

https://doi.org/10.1021/acsami.1c19644
ACS Appl. Mater. Interfaces 2022, 14, 278−296

proved that both Mg^{2+} ions and SO_4^{2-} ions play key roles in the augmented PLQY of $CsMg_xPb_{1-x}I_3$ QDs. This study has also proved that incorporating SO_4^{2-} ions into perovskite synthesis improves stability by causing a steric hindrance effect and eliminates surface traps, resulting in improved optical characteristics with long-term durability. In recent studies, $CsPbBr_3$ QDs with improved PL properties and photostability were synthesized using water additives.[49] Therefore, $CsPbI_3$ NCs were synthesized using water molecules as additives; however, the PL intensity of as-synthesized NCs was found to be water-intolerant, and the emission peak diminished as the amount of water was increased, indicating that H_2O molecules in the $MgSO_4{\cdot}2H_2O$ precursor did not contribute to the enhanced optical properties of $CsMg_xPb_{1-x}I_3$ QDs. Taking this discussion into consideration, the improvement in PLQY of $CsMg_xPb_{1-x}I_3$ QDs could be credited to the synergistic effect of incorporated Mg^{2+} and SO_4^{2-} ions. The role of each ion could be explained as follows: (1) Mg^{2+} ions could reduce the surface defects to some extent, which was supported by increased radiative decay rates, resulting in enhanced PLQY. (2) SO_4^{2-} surface passivation could create a stronger steric effect between the capping ligands and eliminate surface trap states, which is more beneficial to produce high-quality NCs. The other possible mechanism for the improved PLQY of $CsMg_xPb_{1-x}I_3$ QDs is most likely owing to Mg-induced structural stability. Thus, $CsMg_xPb_{1-x}I_3$ QDs have a Goldschmid tolerance factor of 0.93, which is greater than that of $CsPbI_3$ QDs. As a consequence, using a smaller Mg^{2+} dopant in the Pb^{2+} site increases the tolerance factor, which is beneficial for exciton radiative recombination (resulting in a higher PLQY) and improved phase stability. Regardless of radiative recombination, there is a non-radiative relaxation phenomenon that develops in energy loss either by hole trapping or electron trapping. Hence, this could be the reason for the low PLQY of $CsMg_xPb_{1-x}I_3$ QDs with excess $MgSO_4$ dopant. Therefore, the increase in PL lifetime suggests that the addition of a small amount of $MgSO_4$ in $CsPbI_3$ QDs reduces the density of non-radiative recombination centers and surface trap states, simultaneously increases the radiative recombination rate, and eliminates surface trap states as well as the Mg^{2+} and SO_4^{2-} ion incorporation improves the phase stability and leads to a higher steric hindrance effect, respectively, finally resulting in improved PLQY with prolonged stability.

Besides, various PbX_2 (X: Cl, Br, and I) compounds in different proportions were combined with fixed amounts of CsAc and $MgSO_4$ precursors to produce mixed halide perovskite NCs with wavelength-tunable PL intensity in the visible region, as shown in Figure S5. Mg-doped $CsPbX_3$ QD colloidal solution emitted strong light under UV lamp illumination that covers the entire visible spectrum from blue to green to red, as illustrated in Figure S5a. Figure S5b,c depicts the absorption and PL spectra of Mg-doped $CsPbX_3$ NCs, which covered the visible spectral range from 393 to 710 nm, exhibiting a higher absorption coefficient, FWHM (from 14 to 45 nm), and QY (up to 89%). The narrow FWHM values indicate that the NC distribution is homogeneous and that the materials are monochromatic. Moreover, because of the high quantum confinement of NCs, a significant Stokes shift was detected when comparing the absorption spectra with the PL emission spectra. This was obtained from radiative recombination of free exciton or bound exciton recombination. This method is most likely the facile and most straightforward technique to produce highly emissive perovskite QDs with excellent optical properties.

3.3. Synthesis and Characterization of the PQD@Gd Nanoagent. Based on the above optical properties, it is clear that the as-synthesized $CsMg_xPb_{1-x}I_3$ QDs (hereafter referred to as PQDs) can be used as phototherapeutic and imaging agents. However, their solubility in aqueous media is one of the major concerns. To address the increasing demands for imaging-guided therapeutic agents and improve the bioavailability and properties of the $CsMg_xPb_{1-x}I_3$ QDs, we designed and assembled the PQD@Gd theranostic platform, as illustrated in Scheme 1. The PQD@Gd nanoagent was prepared through an encapsulation mechanism at room temperature. First, the PF127-Gd carrier was synthesized by an esterification reaction between the hydroxyl group of PF127 and the carboxylic group of the DTPA-Gd contrast agent using the DCC/DMAP cross-linker, as indicated in Scheme 1. The resulting PF127-Gd conjugates could be employed for encapsulation of hydrophobic drugs due to the amphiphilic nature and MRI response because of the conjugated Gd^{3+} contrast agent. PF127 could self-assemble into a robust micelle structure because of its amphiphilic characteristics, in which the PPO segment (hydrophobic section) of PF127 acts as the core of the micelle via hydrophobic interactions. Thus, the as-synthesized $CsMg_xPb_{1-x}I_3$ QDs were loaded into the hydrophobic core of the PF127-Gd micelle via hydrophobic interactions between the PPO segment of PF127 and a long-chain capping ligand such as OAm, OAc, or TOP (Scheme 1), and the resulting nanoparticles were named as PQD@Gd nanoagents. The hydrophobic interaction was possibly developed. The fabricated PQD@Gd nanoagent exhibited excellent solubility in aqueous solutions by taking advantage of the hydroxyl end of PEO, which is located at the outer edge of the micelle. The as-synthesized PQD@Gd nanoagent demonstrated a spherical micelle or shell-like structure, as shown in TEM profile (Figure S6a). As shown in Figure S6a, several perovskite QDs clustered together inside a micelle structure and maintained their cubic form after polymer embedding, suggesting that the PF127-Gd carrier successfully shielded $CsMg_xPb_{1-x}I_3$ QDs from the aqueous environment. The size distribution of a nanoagent was further analyzed using DLS measurements (Figure S6b), and the results indicated that the average hydrodynamic diameter of PQD@Gd was 315 nm (polydispersity index, PDI = 0.41). The FTIR spectra were recorded to study the surface properties of $CsMg_xPb_{1-x}I_3$ QDs before and after encapsulation. The results shown in Figure S6c demonstrated that $CsMg_xPb_{1-x}I_3$ NCs had strong IR absorption bands at 3400, 2989, 1720, 1212, and 586 cm^{-1}, which could be assigned to stretching frequencies of −OH/−NH, C−H, C═O/C═N, C−O/C−N, and P═O interactions, respectively, due to the presence of the capping ligand. Moreover, the IR peak shown at 1450 cm^{-1} is ascribed to S═O bonding, confirming that SO_4^{2-} acts as a capping ligand to stabilize the surface of perovskites QDs. After encapsulation, because the PF127-Gd polymer is rich in hydroxyl and amine groups, the PQD@Gd nanoagent exhibited a broader IR peak at 3500 cm^{-1}. Furthermore, the shoulder peak at 3002 cm^{-1} is ascribed to the C−H stretching frequency. C═O/C═N stretching, C═C vibration, C−O/C−N stretching, and C−O/C−C stretching were identified in the IR spectra at 1700, 1498, 1389, and 1054 cm^{-1}, respectively. Afterward, the surface charge properties of the PQD@Gd nanoagent were investigated using a zetasizer. The presence of PO_4^{-3}, COO^-, and

https://doi.org/10.1021/acsami.1c19644
ACS Appl. Mater. Interfaces 2022, 14, 278−296

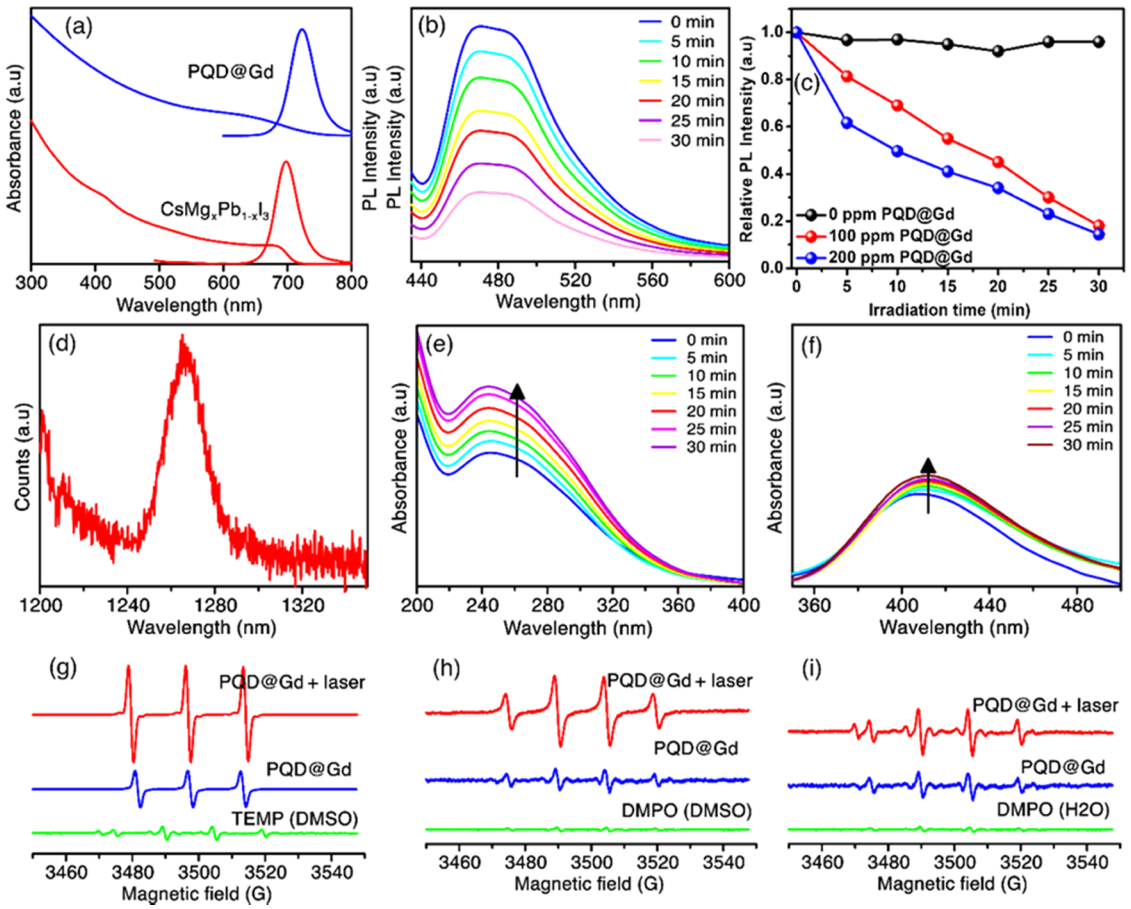

Figure 4. (a) Absorption and PL emission spectra of $CsMg_xPb_{1-x}I_3$ QDs and PQD@Gd nanoagents. (b) PL intensity of 1.5×10^{-3} M DPBF solution ($\lambda_{excitation}$ = 410 nm, $\lambda_{emission}$ = 460 nm) in the presence of 100 ppm PQD@Gd nanoagent at different time intervals upon 671 nm laser irradiation (2.0 W/cm^2). (c) Relative PL intensity of DPBF at 460 nm in the presence of various concentrations of the PQD@Gd nanoagent at different laser irradiation times. (d) Emission spectrum of $^1O_2$ measured at 1270 nm using the PQD@Gd nanoagent (dissolved in D_2O) after 671 nm laser irradiation. Absorption spectra of (e) 100 mM NBT and (f) 10 mM OPD coupled with the PQD@Gd nanoagent upon irradiation with a 671 nm laser at various time intervals. ESR spectroscopic analysis of (g) TEMPO signals in the presence of $^1O_2$ obtained for the PQD@Gd nanoagent with and without laser irradiation. (h) ESR signal for DMPOO adduct formation in the PQD@Gd nanoagent solution with and without laser irradiation for $^{\bullet}O_2^-$ radical detection. (i) DMPOO signal responding to $^{\bullet}OH$ radicals in the presence of the PQD@Gd nanoagent with and without laser illumination.

SO_4^{2-} ions from the capping ligand conferred negative surface charge (−22.68 mV) to $CsMg_xPb_{1-x}I_3$ QDs before encapsulation, as shown in Figure S6d. The PQD@Gd nanoagent displayed a more negative surface charge (−29.09 mV) probably due to the hydroxyl ions of the PF127 polymer, proving that the $CsMg_xPb_{1-x}I_3$ NCs were successfully encapsulated. Figure 4a shows the absorption and PL spectra of $CsMg_xPb_{1-x}I_3$ QDs before and after encapsulation. The absorption spectra of the PQD@Gd nanoagent exhibited a smooth absorption curve at 693 nm, which corresponds to the same position as in the spectra of $CsMg_xPb_{1-x}I_3$ QDs. However, in PL spectra, the PQD@Gd nanoagents demonstrated a considerable shift in the PL peak compared to free $CsMg_xPb_{1-x}I_3$ QDs. This peak shift could be due to the QD aggregation and interdot energy transfer.[50] Furthermore, the PLQY of the PQD@Gd nanoagent was calculated as 53.4%, which is slightly lower than that of non-encapsulated $CsMg_xPb_{1-x}I_3$ QDs (89.1%) suggesting that the encapsulated QDs preserve their intrinsic properties in an aqueous solvent. Time-resolved PL decay lifetimes of $CsMg_xPb_{1-x}I_3$ QDs and PQD@Gd nanoagent were further investigated under the same conditions and compared. The obtained results depicted in Figure S6e indicated that excited electrons possess a relatively long lifetime. The average PL lifetime of the PQD@Gd nanoagent was 23.36 ns (inset of Figure S6e), which is lower compared to 51.89 ns of nonencapsulated $CsMg_xPb_{1-x}I_3$ QDs, indicating that PF127-Gd micelles might result in loss of the surface ligand during the encapsulation mechanism. This would cause the formation of more surface trap states and additional nonradiative channels, thereby resulting in a reduced PL lifetime and lower QY efficiency.

Moreover, the photostability of $CsMg_xPb_{1-x}I_3$ and PQD@Gd nanoagents was investigated by applying UV lamp irradiation at specified time intervals. Figure S6 reveals that the relative PL intensities of $CsMg_xPb_{1-x}I_3$ NCs and PQD@Gd nanoagents were reduced by 34 and 45%, respectively, after 48 h, as compared to the initial PL intensity evaluated at 0 h. The $CsMg_xPb_{1-x}I_3$ NCs (before and after encapsulation) produce bright color after being exposed to UV light for 48 h, as shown in the inset image. This demonstrates that the photoresistance of the $CsMg_xPb_{1-x}I_3$ NCs was comparable before and after encapsulation. Similarly, the moisture durability of $CsMg_xPb_{1-x}I_3$ QDs before and after encapsulation was examined using a 10% volume ratio of DI water. The

https://doi.org/10.1021/acsami.1c19644
ACS Appl. Mater. Interfaces 2022, 14, 278−296

fluorescence intensity of $CsMg_xPb_{1-x}I_3$ QDs deteriorated immediately, with only 12% of the initial intensity remaining after 40 min, whereas the PQD@Gd nanoagent retained 41% of its initial intensity even after 24 h. Furthermore, as illustrated in the inset picture of Figure S6g, $CsMg_xPb_{1-x}I_3$ NCs deteriorated in the presence of 10% DI water, while the PQD@Gd nanoagent shows a luminous image, demonstrating that encapsulated NCs retain their luminescent properties in the aqueous solvent. The results show that the aqua-resistant properties of $CsMg_xPb_{1-x}I_3$ QDs enhanced after encapsulation.

3.4. Photodynamic Therapy of the PQD@Gd Nanoagent. The PNCs are ideal candidates to be employed as photosensitizers (PSs) in light-activated therapeutic activities, such as photodynamic therapy, because of their multiple excitonic generation properties. In PDT, the PS absorbs the light and excites to the triplet state; from there, it decomposes molecular oxygen to reactive oxygen species (ROS).[1,40] Thus, herein, we studied the suitability of the PQD@Gd nanoagent to be employed as a PDT agent by measuring the ROS generation under laser irradiation. The widely used DPBF probe was employed for the detection of ROS. The yellowish fluorescent DPBF degrades to colorless 1,2-dibenzoylbenzene (DBB) upon interaction with ROS species (Figure S7a); thus, its emission spectra at 460 nm ($\lambda_{excitation}$ = 410 nm) is helpful to evaluate the ROS generation. As shown in Figure S7b, the PL spectra of DPBF remained unchanged after 30 min laser irradiation. However, the PL intensity of DPBF gradually declined as the irradiation time increased (Figure 4b) in the presence of 100 ppm PQD@Gd nanoagent, indicating that PQD@Gd could serve as an efficient ROS-generating PS agent. The influence of PQD@Gd nanoagent concentration on ROS production efficiency was investigated, as shown in Figure S7c. At higher concentrations (200 ppm) of PQD@Gd, the fluorescence intensity of DPBF declined rapidly due to the generation of more ROS. In the presence of 200 ppm of PQD@Gd, around 75% fluorescence intensity declined from the initial value within 15 min of irradiation, whereas 100 ppm PQD@Gd caused a 68.5% decline in the same irradiation time (Figure 4c), implying that ROS generation is concentration-dependent. Next, to validate $^1O_2$ radicals, the PL emission spectra were recorded at around 1270 nm ($\lambda_{excitation}$ = 671 nm). The PQD@Gd sample was first saturated with O_2 gas for 10 min before being irradiated with a laser at 671 nm, and then, the PLspectrum was recorded at $\lambda_{excitation}$ = 671 nm. A strong and intense peak at 1265 nm with a bandwidth of 20.8 nm was observed (Figure 4d), which confirms the generation of $^1O_2$ radicals. The ROS produced from the light-activated PQD@Gd nanoagent was further analyzed using NBT and OPD colorimetric assays to validate the presence of $^{\bullet}O_2^-$ and $^{\bullet}OH$ radical species, respectively. In the UV−vis spectra of NBT and PQD@Gd mixture (Figure 4e), the intensity of the characteristic peak of reduced NBT at 260 nm gradually increased with increasing irradiation time and also the formation of gray formazan was observed (as shown in Figure S8a). indicating the formation of $^{\bullet}O_2^-$ radicals via a charge transfer mechanism. In the UV−vis spectra of the mixture of PQD@Gd and OPD solution (as shown in Figure 4f), the absorbance of the peak at 450 nm, which is the characteristic peak of formed DAP (Figure S8b), increased with irradiation time, indicating that $^{\bullet}OH$ radicals formed via an energy transfer mechanism. These experimental results confirmed that the PQD@Gd nanoagent predominantly produces $^1O_2$ and $^{\bullet}O_2^-$ radicals and a small amount of $^{\bullet}OH$ radicals.

The ability of the PQD@Gd nanoagent to generate ROS was further examined qualitatively using ESR spectroscopy. In this regard, TEMP and DMPO were used as probes for detection of $^1O_2$ and $^{\bullet}O_2^-$/$^{\bullet}OH$, respectively. Figure 4g shows that no signal peak was obtained for TEMP only after 10 min of laser irradiation. However, the combination of PQD@Gd with TEMP produced a set of characteristic TEMP-1-oxyl (TEMPO) signal peaks with a ratio of 1:1:1 in the absence of the laser. This phenomenon was significantly pronounced when the PQD@Gd nanoagent was exposed to 10 min laser irradiation, which was attributed to the generation of $^1O_2$. Similar results were obtained when DMPO in DMSO was used for the detection $^{\bullet}O_2^-$. No signals were observed for DMPO only with the laser and DMPO with PQD@Gd, as shown in Figure 4h. However, under 671 nm laser irradiation, the ESR spectra of DMPO and PQD@Gd exhibited signal peaks at 1:2:2:1 ratio due to the formation DMPOO adducts, confirming that the as-synthesized nanoagent generated light-induced $^{\bullet}O_2^-$ radicals. For the detection of hydroxyl ($^{\bullet}OH$) radicals, DMPO in water was used as the probe. Consistent with the above trends, neither the control experiment (DMPO in water) nor the PQD@Gd nanoagent produced an ESR signal without the laser (Figure 4i). The combination of the PQD@Gd nanoagent and laser irradiation generated a weak ESR peak (with a ratio of 1:2:2:1) due to the formation of DMPOO, approving $^{\bullet}OH$ radical generation. According to the results of ESR spectroscopy and colorimetric assay, the most abundant radical species generated by the PQD@Gd nanoagent were $^1O_2$ and $^{\bullet}O_2^-$ with a low proportion of $^{\bullet}OH$ radicals. To understand the mechanism of efficient ROS generation from the PQD@Gd nanoagent, the multiple exciton property of perovskite QDs was reported. In the literature, it was reported that perovskite QDs owned higher light-harvesting property, which could find application in many photocatalysis processes. Therefore, the absorption of light by PNCs causes formation of an electron−hole pair (e^-, h^+), as well as the subsequent separation and recombination of electrons and holes is the most possible pathway for the light-activated ROS generation property. Briefly, PNCs + $h\nu \rightarrow e^- + h^+$, and then, the photogenerated electrons and holes undergo a self-trapping process to produce e_{TR}^- and h_{TR}^+ species, respectively. After that, the recombination of electron−hole pairs occurred, $e_{TR}^- + h_{TR}^+ \rightarrow e_{CB}^-$ + heat, which is more favorable for oxygen-based radical species. The formation of electrons and holes in the system results in catalysis of molecular oxygen and/or water molecules to produce ROS via energy and charge transfer mechanisms, as shown in Figure S8c. Overall, our results are in good agreement with a recent report, approving that the PQD@Gd nanoagent could be used as a PS agent in PDT treatment of various cancer cells.[1,51]

3.5. Photocatalytic Evaluation of the PQD@Gd Nanoagent. The photocatalytic efficiency of as-synthesized PQD@Gd nanoagents was demonstrated by deactivation of organic pollutants under visible light illumination. Redox processes mediated by photoinduced electrons (e^-) and holes (h^+) on the photocatalyst's surfaces produce photocatalytic properties.[52,53] In light of this, UV−vis spectroscopy was used to demonstrate the degradation of MO, RhB, and MB dyes under laser illumination.

As shown in Figure S9, there was no substantial change in the absorption spectra of dyes in the presence of only laser or only PQD@Gd nanoagent, implying that the PQD@Gd nanoagent is a light-activated catalyst. In the presence of the

https://doi.org/10.1021/acsami.1c19644
ACS Appl. Mater. Interfaces 2022, 14, 278−296

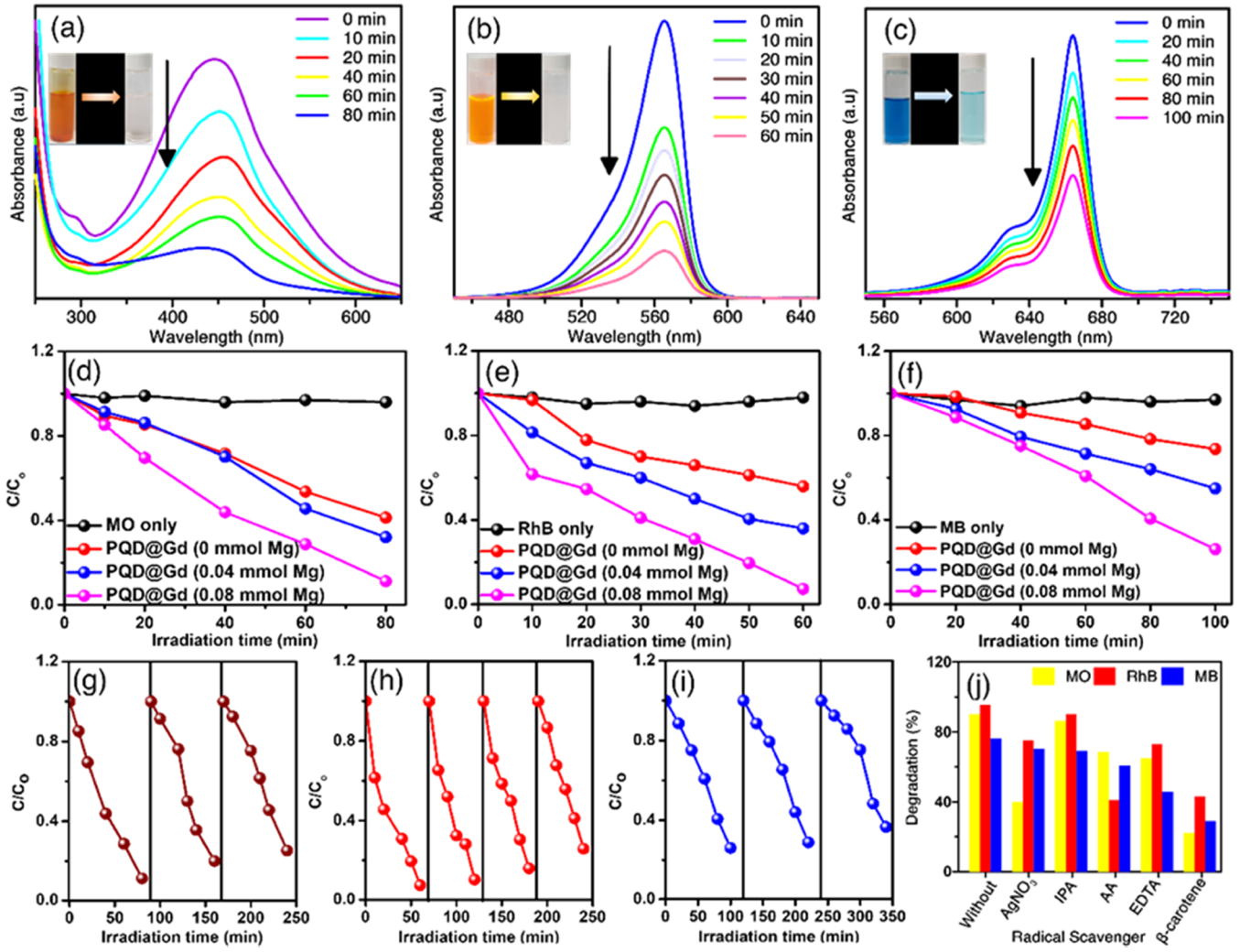

Figure 5. Absorption spectra of light-induced degradation of (a) 1 mM MO, (b) 1 mM RhB, and (c) 1 mM MB using the PQD@Gd nanoagent. Relative concentrations of (d) MO, (e) RhB, and (f) MB organic dyes upon combining with the PQD@Gd photocatalyst at different Mg contents. Reusability performance of the PQD@Gd photocatalyst toward the decomposition of (g) MO, (h) RhB, and (i) MB organic dyes. (j) Photodegradation of Mo, RhB, and MB organic dyes by the PQD@Gd photocatalyst examined with different radical scavengers. The control experiment was performed in the absence of a radical scavenger. The experiment was performed using 671 nm light illumination (2.0 W/cm^2).

PQD@Gd nanoagent, the absorbance of characteristic peaks of MO, RhB, and MB at 460, 560, and 660 nm, respectively, gradually decreased as the irradiation time increased (Figure 5a−c). Also, the color of the solution changed to colorless for MO and RhB dye solutions and light blue for MB dye solution (inset in Figure 5a−c), indicating the complete degradation of MO and RhB due to the photocatalytic activity of the nanoagents. As a result, the amount of remaining dyes in the solution became lesser with increasing concentration of the nanoagent or irradiation time (Figure S10a−c), intimating that the catalytic activity depends on the laser irradiation time and PQD@Gd nanoagent concentration.

Next, the effect of Mg^{+2} ion doping on photocatalytic activity was studied by employing the PQDs that were prepared with different amounts of Mg precursors. As shown in Figure 5d−f, at any irradiation time point, the dye degradation rate increased with increasing Mg content in PQDs. After 80 min irradiation, 58.7, 67.9, and 88.8% of MO was degraded for PQDs with 0, 0.04, and 0.08 mmol Mg, respectively. Similarly, 44.1, 64, and 92.7% photodegradation of the RhB dye was observed for PQDs with 0, 0.04, and 0.08 mmol Mg, respectively, after 60 min laser irradiation. For MB, 26.4, 45.1, and 73.9% degradation occurred after 100 min of continuous laser irradiation. These findings validated that doping Mg^{+2} ions into $CsPbI_3$ QDs significantly enhanced the catalytic activities of resulting $CsMg_xPb_{1-x}I_3$ QDs. Pradeev Raj et al. and Yousefi et al. recently reported that the photocatalytic activity of Mg-integrated ZnO nanoparticles was increased, and the dye-degrading activity was dependent on the Mg dopant's concentration.[54,55] The minor shift in the absorption spectra of the $CsMg_xPb_{1-x}I_3$ QDs in Figure 3a could be due to the slightly grown crystal size, which is beneficial for the improved light-harvesting efficiency caused by enhanced light scattering properties. Another argument is that after Mg^{2+} doping, the band gap difference decreased (Figure 3f), causing electron−hole recombination to accelerate radical generation, thereby triggering the photodegradation activity. The addition of Mg^{2+} ions to the QD structure boosted the light absorption capacity, which could promote the formation of more radical species and increase the efficiency of organic dye degradation.

The reaction mechanism for the pollutant's degradation is shown in Figure S11. The combination of a light source and

https://doi.org/10.1021/acsami.1c19644
ACS Appl. Mater. Interfaces 2022, 14, 278−296

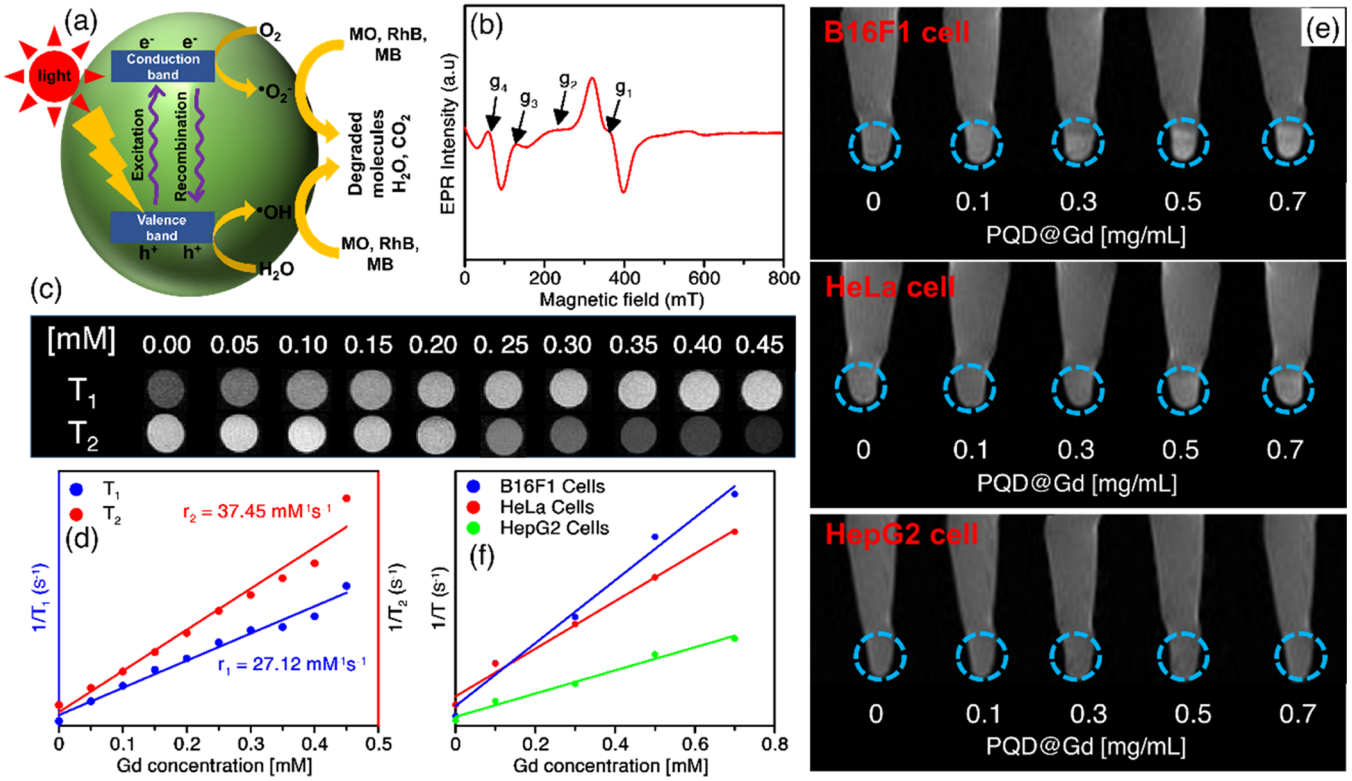

Figure 6. (a) Schematic illustration of a proposed mechanism for the photocatalytic activity of the PQD@Gd nanoagent. (b) ESR spectra of the PQD@Gd nanoagent measured at 10 K. (c) Representative T_1- and T_2-weighted phantom pictures of the PQD@Gd sample at different Gd^{3+} concentrations. (d) Plot of water−proton longitudinal $(1/T_1)$ and transverse $(1/T_2)$ relaxation rates versus different Gd^{3+} concentrations based on panel (c). (e) T_1- and T_2-weighted MR pictures of B16F1, HeLa, and HepG2 cancer cells cultured with various amounts of the PQD@Gd nanoagent overnight. (f) Plot of inverse relaxation rate $(1/T)$ versus different Gd^{3+} contents depending on panel (e). The slope of fitted lines was used to compute the relaxivity value.

the PQD@Gd nanoagent could result in the generation of radical species, which would activate the breakdown of the MO structure into two benzyl rings (Figure S11a). For the RhB dye, the radical species would possibly reduce it to rhodamine, as shown in Figure S11b. The RhB dye can decompose in a number of ways, including through an indirect reaction with powerful oxidants that were generated photocatalytically from water on the surface of the PQD@Gd nanoagent or explicitly through the decay of the RhB dye adsorbed to the surface of PQD@Gd. Because it contains four *N*-ethyl groups on both sides of the xanthene moiety, the RhB dye could bind to the surface of PQD@Gd via electrostatic coupling. In the case of MB, the oxidative breakdown of MB to CO_2 or the reductive degradation of MB to the colorless Leucomethylene blue could be a plausible mechanism for MB degradation (Figure S11c). Furthermore, the durability of the PQD@Gd nanoagent (0.08 mmol Mg content) photocatalyst toward MO, RhB, and MB was also explored, as shown in Figure 5g−i. After three repeated cycles, the percentage of the dye degraded was slightly decreased to 75% from 89.01% for MO, 74% from 92.2% for RhB, and 63% from 74% for MB, proving that the PQD@Gd nanoagent had superior photocatalytic performance and comparable recyclability. To identify the type of radicals responsible for the degradation mechanism, we used a radical trapper such as isopropanol for $^{\bullet}OH$, EDTA for e^-, *β*-carotene for $^1O_2$, $AgNO_3$ for h^+, and ascorbic acid for $^{\bullet}O_2^-$. Figure 5j shows that the degrading capacity of the PQD@Gd nanoagent (0.08 mmol Mg content) against MO and MB dyes decreased from 89.12% (without the trapper) to 22.12 and 29.8% for the *β*-carotene reagent, respectively, indicating that the decomposition of MO and MB dyes was catalyzed by singlet oxygen ($^1O_2$). Using $AgNO_3$ and EDTA as radical trappers, the degradation rate of MO and MB dyes reduced by 45%, revealing that photogenerated electrons and holes accelerate the breakdown of the pollutants. The photodegrading capacity of PQD@Gd for RhB reduced to 41% when ascorbic acid and *β*-carotene were used as radical trappers, confirming that $^{\bullet}O_2^-$ and $^1O_2$ radicals were preferable to inactivate RhB structures.

The underlying mechanism for the degradation of organic dyes can be explained as follows: the photocatalysis reaction could be triggered when a high-energy photon with sufficient energy (corresponding to the E_{bg} of the photocatalyst) was absorbed, and charge separation could occur when an electron (e) was driven from VB to CB, as illustrated in Figure 6a. In the VB and CB, a hole (h^+) and an electron (e^-), which are potential oxidizing and reducing agents, respectively, could be produced via the following reaction: photocatalyst + $h\nu \rightarrow e^- + h^+$. The h^+ could directly oxidize the pollutant or water to produce $^{\bullet}OH$ radicals, which subsequently oxidized the pollutants and the resulting degraded products. The electron in the CB could reduce the molecular oxygen adsorbed on the photocatalyst surface, forming reactive superoxide radicals ($^{\bullet}O_2^-$) that inactivated the organic molecules. The ESR data strongly supported this explanation, i.e., $^1O_2$, $^{\bullet}O_2^-$, and $^{\bullet}OH$ radicals are responsible for photocatalytic degradation of MO, RhB, and MB, respectively. In ESR spectroscopy, generation of $^1O_2$ radicals and $^{\bullet}O_2^-$ and $^{\bullet}OH$ radicals was detected using TEMP and DEMPO, respectively (Figure 4d−f). These results

https://doi.org/10.1021/acsami.1c19644
ACS Appl. Mater. Interfaces 2022, 14, 278−296

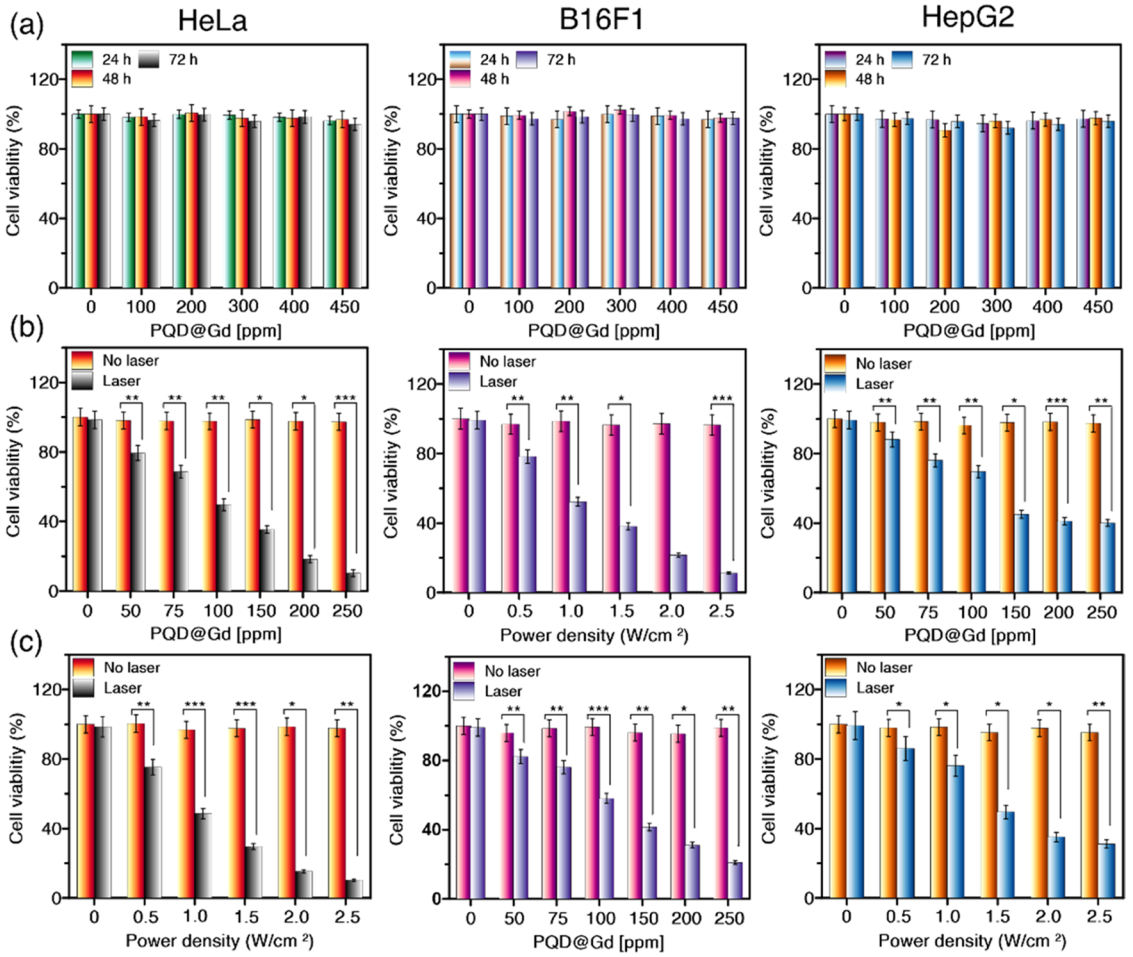

Figure 7. (a) In vitro biocompatibility of the PQD@Gd nanoagent incubated at different concentrations with HeLa, B16F1, and HepG2 cancer cells for 24, 48, and 72 h. (b) In vitro PDT treatment of HeLa, B16F1, and HepG2 cancer cells incubated with various amounts of the PQD@Gd nanoagent overnight and treated with a 671 nm laser power (2.0 W/cm^2) for 5 min. (c) In vitro PDT treatment of HeLa, B16F1, and HepG2 cancer cells incubated with 200 ppm of PQD@Gd nanoagent overnight and irradiated with a 671 nm laser source at various power densities (0.5, 1.0, 1.5, 2.0, and 2.5 W/cm^2) for 5 min.

are consistent with those in Figure 5j, confirming that the as-synthesized PQD@Gd nanoagents could act as photocatalyst agents in various wastewater treatment techniques or bacterial inactivation protocols.

3.6. MRI Measurements of the PQD@Gd Nanoagent.

The presence of paramagnetic metal ions Gd^{3+} could endow the PQD@Gd nanoagent with MRI properties. According to the literature, the Gd^{3+} ion with seven unpaired electrons, outstanding magnetic properties, and a high electron-spin relaxation time could be used as a T_1-dominating contrast agent in various cancer treatments.[56,57] Thus, ESR spectroscopy was employed to confirm the presence of unpaired electrons in Gd^{3+} of PQD@Gd. As displayed in Figure 6b, a single prominent peak and Zeeman interaction with g_1 = 1.99, g_2 = 2.48, g_3 = 2.8, and g_4 = 3.00 was observed, indicating that PQD@Gd nanoagents could be promising candidates for MR imaging. These findings are in accordance with earlier findings of Gd-based MRI agents.[56,58] The Gd^{3+} ion can promote longitudinal (spin-lattice relaxation) or transverse (spin−spin relaxation) relaxation, allowing it to be used as a T_1 or T_2 contrast agent. Thus, the relaxivities of PQD@Gd nanoagents in aqueous media were measured to assess the feasibility of using them as dual T_1- and T_2-weighted contrast agents. Figure 6c depicts the T_1 and T_2-weighted MR images of PQD@Gd nanoagents at various concentrations based on Gd contents, indicating a concentration-dependent signal enhancement for both T_1- and T_2-weighted images. Briefly, the T_1 phantom weighted image displayed a more brighter contrast with increasing Gd^{3+} concentration, whereas under the same conditions, T_2 studies displayed darker spot images, implying that the PQD@Gd nanoagent could be used as a dual-modal contrast agent in cancer diagnosis. Generally, the efficiency of an MRI contrast agent is assessed by the following equation: $R_{1,2} = \frac{1}{T_{1,2}^i} + r_{1,2} \times C$, where $R_{1,2}$ is the measured relaxation rate (s^{-1}) of MRI contrast agents, T is the observed relaxation rate (s^{-1}) before the addition of contrast agents, $r_{1,2}$ is the relaxivity coefficient (mM^{-1} s^{-1}), and C is the concentration (mM) of the MRI contrast agents. Positive MR contrast agents with high r_1 values and r_2/r_1 ratios of 1−2 is optimal, while negative MR contrast agents with high r_2 values and r_2/r_1 ratios larger than 10 are preferred. Specifically, T_1 contrast agents help to strengthen the longitudinal regression value, resulting in a positive (bright) contrast in the selected spot, whereas T_2 contrast agents (darker contrast) boost the signal intensity in T_2-weighted pictures.[59,60] The relaxivity coefficients (r_1 and r_2) were computed from T_1 and T_2 mapping images obtained using an inversion recovery sequence to evaluate the MR

https://doi.org/10.1021/acsami.1c19644
ACS Appl. Mater. Interfaces 2022, 14, 278−296

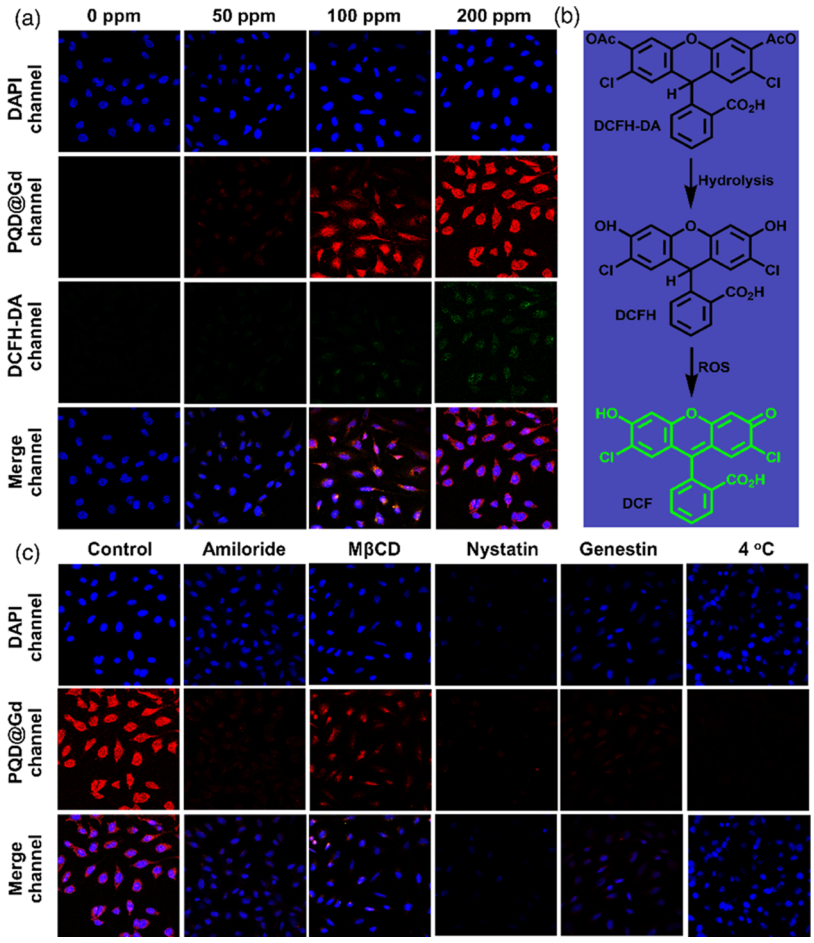

Figure 8. (a) Confocal images of HeLa cells incubated with various concentrations of the PQD@Gd nanoagent for 6 h at 37 °C and in a humidified atmosphere. The cancer cells were stained with DAPI (blue dye) to track the nucleus. The green channel indicates the DCFH-DA oxidation to DCF• species. The cancer cells were treated with the DCFH-DA reagent and illuminated under 671 nm laser power (2.0 W/cm^2). (b) Hydrolysis and ROS-induced oxidation of DCFH-DA molecules to form DCF green fluorescent material. (c) Cellular imaging of HeLa cells incubated with 30 μL of different inhibitors (nystatin, genistein, amiloride, and MβCD) for 30 min and 200 ppm of PQD@Gd nanoagent 3 h. For the temperature-dependent study, HeLa cells were incubated with 200 ppm of PQD@Gd nanoagent at 4 °C. The control experiment was performed without adding the inhibitor. The images were captured at excitation wavelengths of 405, 488, and 532 nm for blue, green, and red channels, respectively.

contrast effect, as shown in Figure 6d. The r_1 and r_2 values of the PQD@Gd nanoagent were estimated to be 27.12 and 37.45 mM^{-1} s^{-1}, respectively. The ratio of r_1 and r_2 was calculated to evaluate the potential of the nanoagent in terms of T_1 and T_2 contrast effects. The r_2/r_1 ratio was found to be 1.38, confirming that the PQD@Gd nanoagent could be a promising candidate in T_1-guided imaging application, but the higher relaxivity value (r_2 = 37.45 mM^{-1} s^{-1}) made them also preferable as T_2 contrast agents. The results are in good agreement with a recent report.[56,57]

After confirming the T_1-dominating contrasting effect of the PQD@Gd nanoagent, in vitro MRI studies were performed using cancer cells to verify the ability of the PQD@Gd nanoagent as a dual T_1/T_2 MR agent in cancer diagnosis. In this regard, cancer cells were treated with a concentration gradient of the PQD@Gd contrast agent overnight, and subsequently, MRI measurements were performed. Figure 6e shows the longitudinal (T_1)- and transverse (T_2)-weighted images of the different cancer cells such as B16F1, HeLa, and HepG2. The nontreated cells served as a control group. Compared with the control group, the B16F1 and HeLa cancer cells treated with the PQD@Gd nanoagent showed obvious T_1 MRI signals and the T_1 value increased with increasing PQD@Gd concentrations, confirming the T_1-dominating effect, whereas HepG2 cancer cells treated with the PQD@Gd nanoagent did not show any significant change with increasing material concentration. These findings indicated that the PQD@Gd nanoagent offered a superior positive T_1 contrast enhancement for in vitro MR imaging. This was further confirmed by plotting the relaxivity properties against different concentrations of the PQD@Gd nanoagent (Figure 6f), proving that the relaxation value (r_1) increased with increasing PQD@Gd concentration for B16F1 and HeLa cancer cells. When the T_1- and T_2 contrast signals were comparable, the dual contrast effect probes may produce ideal contrasts on both T_1- and T_2-weighted images due to their synergistic combination of the two relaxation effects. The accumulation of the PQD@Gd nanoagent in the cancer cells via the endocytosis route led to the considerable change in the contrasting intensity.

3.7. In Vitro Demonstration of the PQD@Gd Nanoagent. In vitro cytotoxicity of the PQD@Gd nanoagent was assessed using the WST-1 assay. First, the cytocompatibility of the PQD@Gd nanoagent to HeLa, HepG2, and B16F1 cancer

https://doi.org/10.1021/acsami.1c19644
ACS Appl. Mater. Interfaces 2022, 14, 278−296

cells was examined. As shown in Figure 7a, at all given concentrations, the viability of cells treated with the PQD@Gd nanoagent was comparable to that of untreated cells, suggesting that the PQD@Gd nanoagent is cytocompatible. This could be because of the encapsulation into the PF127 micelle structure, which could protect the cell by preventing the release of harmful Pb^{2+} ions. Next, the anticancer PDT effect of the PQD@Gd nanoagent was investigated under light illumination. To this end, the cancer cells were treated overnight with various concentrations of the nanoagent (0, 50, 75, 100, 150, 200, and 300) and irradiated using a 671 nm laser (2.0 W/cm^2). Without light irradiation, the nanoagent alone did not induce cell toxicity even at a concentration as high as 250 ppm. On the other hand, under light irradiation, the cell viability decreased with increasing concentration of the nanoagent (Figure 7b) because the endocytosed PQD@Gd nanoagent generated ROS upon laser irradiation. The anticancer efficacy of most substances is commonly expressed using the IC_{50} value, which indicates the amount of a drug required to inhibit a biological process by 50%. Thus, the cell viability relative to the PQD@Gd concentration was fitted with a logistic function, and the IC_{50} values of PQD@Gd for HeLa, B16F1, and HepG2 were calculated as 100, 123, and 117 ppm, respectively. According to Figure 7b, PQD@Gd induced higher cell death in B16F1 and HeLa cells than that in HepG2 cells. At 250 ppm of PQD@Gd and 5 min of laser irradiation, the cell death was around 85% for B16F1 and HeLa cells, whereas the cell death for HepG2 was 60%. The internalization of the PQD@Gd nanoagent is predicted to be stronger in B16F1 and HeLa cells, resulting in a stronger PDT impact. Moreover, as depicted in Figure 7c, the experiments were carried out using various power densities (0.5, 1.0, 1.5, 2.0, and 2.5 W/cm^2) and a constant PQD@Gd nanoagent concentration (200 ppm). The cell viability decreased as the power density increased due to the generation of more ROS at higher power densities. After being treated with the 200 ppm PQD@Gd nanoagent and a 2.5 W/cm^2 laser power, the live cell numbers for HeLa and B16F1 cancer cells reduced to 8.9 and 9.1%, respectively, whereas 31.5% of HepG2 cells remained alive in the same circumstances, implying that the PDT efficiency was concentration- and laser-dependent. The findings were in accordance with the qualitative analysis shown in Figure 4c, confirming that the as-synthesized PQD@Gd nanoagent could be a potential anticancer agent.

3.8. In Vitro Fluorescence Imaging. The ionic instability and degradation of PQDs in water are the main hurdles in their applicability in cellular imaging. However, as the stability and water dispersibility of PQDs were improved by our strategy, the resulting PQD@Gd nanoagents might be used as luminescent probes for biological imaging. To investigate the applicability of the PQD@Gd nanoagent as fluorescent biomarkers in practical nanomedicine, cellular internalization of the PQD@Gd nanoagent was demonstrated using HeLa, B16F1, and HepG2 cancer cells. The cancer cells were supplied with various amounts of the PQD@Gd nanoagent overnight in a humidified atmosphere and then stained with DAPI to track the nucleus. The confocal images of HeLa cells treated with PQD@Gd shown in Figure 8a exhibited bright red fluorescence, confirming that PQD@Gd nanoagents were well absorbed into the cells. Moreover, the fluorescence intensity increased with increasing concentration of nanoagents, implying that the cellular uptake may be controlled by a concentration gradient. Similar results were obtained for B16F1 and HepG2 cancer cells; however, the intensity was low in HepG2 compared to that in B16F1 cells under similar conditions (Figure S12), suggesting that the nanoagents were preferably uptaken by B16F1 and HeLa cells. Further, to determine the position of the nanoagent in the organelles of the cancer cells, confocal scans with *Z*-axis stacking were performed under the same conditions. The three-dimensional confocal images of HeLa, B16, and HepG2 cells incubated with the PQD@Gd nanoagent obtained under the vertical scan mode along the *Z*-axis are shown in Figures S13−S15. The results indicated that PQD@Gd was well distributed in the cell structure, as higher QD signals were observed in the cytoplasm than on the cell surface. Therefore, the *Z*-stack images (from top to bottom) showed effective integration of PQD@Gd in HeLa, B16, and HepG2 cells and highlighted the differences in FL signals between cell lines. The fluorescence intensities were quantified and compared using ImageJ analysis. Figure S16a shows that B16F1 and HeLa cells had higher QD signals, proving that PQD@Gd is well distributed in the cell, whereas HepG2 cancer cells showed lower signals under similar conditions due to the lower diffusion rate of the PQD@Gd nanoagent. The CLSM and MR imaging analyses validated that the PQD@Gd nanoagent is suitable for both MRI and bioimaging, enabling them as potential candidates for dual-mode cancer cell diagnosis.

3.9. Intracellular ROS Detection. After the cellular uptake of PQD@Gd was validated, the ability of PQD@Gd to regulate the intracellular oxidative stress upon irradiation with a laser was examined using a DCFH-DA probe. Under intracellular oxidative stress, the non-fluorescent DCFH-DA converts to green fluorescent 2′,7′-dichlorofluorescein (DCF), as shown in Figure 8b.[61] The nucleus was stained with DAPI. According to the CLSM photographs shown in Figure 8a, the HeLa cells treated with only laser without the PQD@Gd nanoagent exhibited a weak green fluorescence (FL) signal. However, the cells treated with the laser and PQD@Gd nanoagent exhibited higher green fluorescence signals than the control cells, suggesting the generation of intracellular ROS due to the PDT effect of PQD@Gd. The green fluorescence signal became brighter with increasing PQD@Gd nanoagent concentration, validating that the PDT response was laser-induced and concentration-dependent. The distribution of PQD@Gd in the nucleus seems to be confirmed by the overlap of blue, red, and green signals in the provided overlay images. Moreover, in Figure 8a, the degree of ROS formation (green fluorescence) correlates with the cell toxicity results, suggesting that PQD@Gd effectively targets HeLa cells. This quantitative result indicates that the PQD@Gd nanoagent is preferentially uptaken by cancer cells, suggesting that it could be used as a multifunctional platform FL and MRI probe as well as a PDT agent for cancer diagnosis and therapy.

The mechanism of intracellular uptake was further investigated with different inhibitors, as mentioned in Section 2. In this study, HeLa cancer cells were cultured with different inhibitors such as amiloride, nystatin, genistein, and MβCD for 30 min and then with 200 ppm of PQD@Gd nanoagent for 3 h. The CLSM images shown in Figure 8c demonstrated that the genistein inhibitors significantly suppressed the nanoagent uptake, indicating that the caveolae-mediated endocytosis pathway played a major role. Notably, the inhibitors amiloride and nystatin facilitated less nanoagent uptake than the MβCD inhibitors, which had approximately the same mean fluorescence intensity (Figure S16b) as the control experiment

https://doi.org/10.1021/acsami.1c19644
ACS Appl. Mater. Interfaces 2022, 14, 278−296

(without the inhibitor). Remarkably, none of the inhibitors completely stopped the uptake process, suggesting that the nanoagents are endocytosed via multiple pathways simultaneously. In addition, the cells maintained at a lower temperature showed extremely limited uptake, suggesting that the endocytosis process is energy-dependent rather than diffusion-driven across the cell membrane.

4. CONCLUSIONS

In summary, we have prepared Mg^{+2} ion-doped $CsPbI_3$ QDs ($CsMg_xPb_{1-x}I_3$ QDs) with improved optical properties and controllable morphology via the microwave technique. The $CsMg_xPb_{1-x}I_3$ NCs had higher PLQY (~89%) and improved phase stability than undoped $CsPbI_3$ NCs because of the improved charge recombination rate and increased Goldschmidt tolerance factor caused by Mg doping. Subsequently, the as-synthesized $CsMg_xPb_{1-x}I_3$ NCs are further encapsulated into the micelle-like structure of PF127-Gd through hydrophobic−hydrophobic interactions to improve their bioapplicability. The resulting PQD@Gd nanoagents have demonstrated good water dispersibility due to the presence of hydrophilic PF127 on the surface. The capabilities of PQD@Gd to generate ROS and degrade organic dyes photocatalytically were investigated under light irradiation. The T_1 and T_2 contrast measurement studies suggested that the PQD@Gd nanoagent could be a promising theranostic agent in cancer diagnosis. In vitro results showed that the PQD@Gd nanoagents are taken up by the different cancer cells via caveolae-mediated endocytosis pathways and effectively damaged the cancer cells upon laser irradiation through ROS-mediated therapy. Confocal imaging and MRI proved that the nanoagent produced excellent fluorescent imaging and contrast ability, respectively. Taking all this together, the red-emitting PQD@Gd multifunctional nanoagent could be employed as a fluorescent and MRI-guided PDT agent in future nanomedicine. The photocatalytic activity of the PQD@Gd nanoagent sheds light on its use in different antibacterial inactivation experiments.

■ ASSOCIATED CONTENT

Supporting Information

The Supporting Information is available free of charge at https://pubs.acs.org/doi/10.1021/acsami.1c19644.

Microwave synthesis of $CsPbI_3$ and $CsMg_xPb_{1-x}I_3$ QDs; optical band gap energies of $CsPbI_3$ and $CsMg_xPb_{1-x}X_3$ QDs; PL emission spectra of $CsPbI_3$ and $CsMg_xPb_{1-x}I_3$ QDs in different conditions; DLS measurements of $CsPbI_3$ and $CsMg_xPb_{1-x}I_3$ QDs; fluorescence lifetimes of $CsPbX_3$ and $CsMg_xPb_{1-x}X_3$ QDs; TEM images, DLS analyses, FTIR spectra, and ζ-potentials of $CsMg_xPb_{1-x}I_3$ QDs and PQD@Gd nanoagents; photocatalytic degradation of MO, RhB, and MB organic dyes in the presence of the PQD@Gd nanoagent; CLSM images of the cancer cells labeled with different concentrations of the PQD@Gd nanoagent; and comparison of the fluorescence intensity of cellular imaging versus PQD@Gd concentration (PDF)

■ AUTHOR INFORMATION

Corresponding Author

Jia-Yaw Chang − *Department of Chemical Engineering, National Taiwan University of Science and Technology, Taipei 10607 Taiwan, Republic of China; Taiwan Building Technology Center, National Taiwan University of Science and Technology, Taipei 10607 Taiwan, Republic of China;* orcid.org/0000-0002-4172-6612; Phone: +886-2-27303636; Email: jychang@mail.ntust.edu.tw; Fax: +886-2-27376644

Authors

Girum Getachew − *Department of Chemical Engineering, National Taiwan University of Science and Technology, Taipei 10607 Taiwan, Republic of China;* orcid.org/0000-0003-0054-0712

Chiranjeevi Korupalli − *Department of Chemical Engineering, National Taiwan University of Science and Technology, Taipei 10607 Taiwan, Republic of China;* orcid.org/0000-0002-8855-9938

Akash S. Rasal − *Department of Chemical Engineering, National Taiwan University of Science and Technology, Taipei 10607 Taiwan, Republic of China;* orcid.org/0000-0003-4630-7772

Worku Batu Dirersa − *Department of Chemical Engineering, National Taiwan University of Science and Technology, Taipei 10607 Taiwan, Republic of China*

Mochamad Z. Fahmi − *Department of Chemistry, Universitas Airlangga, Surabaya 60115, Indonesia;* orcid.org/0000-0001-5430-9992

Complete contact information is available at: https://pubs.acs.org/10.1021/acsami.1c19644

Notes

The authors declare no competing financial interest.

■ ACKNOWLEDGMENTS

The authors acknowledge the financial support from the Ministry of Science and Technology of the Republic of China (Contract Nos. MOST 108-2218-E-011-017-MY3 and 110-2113-M-011-003). This work was also financially supported by Taiwan Building Technology Center through the Featured Areas Research Center Program within the framework of the Higher Education Sprout Project by the Ministry of Education in Taiwan. The authors thank C.-Y. Chien of the Ministry of Science and Technology (National Taiwan University) for assistance in TEM experiments.

■ REFERENCES

(1) Gu, K.; Wang, Y.; Shen, J.; Zhu, J.; Zhu, Y.; Li, C. Effective Singlet Oxygen Generation in Silica-Coated CsPbBr3 Quantum Dots through Energy Transfer for Photocatalysis. *ChemSusChem* **2020**, *13*, 682−687.

(2) Shi, R.; Waterhouse, G. I.; Zhang, T. Recent Progress in Photocatalytic CO2 Reduction Over Perovskite Oxides. *Solar RRL* **2017**, *1*, No. 1700126.

(3) Xu, Y.-F.; Yang, M.-Z.; Chen, B.-X.; Wang, X.-D.; Chen, H.-Y.; Kuang, D.-B.; Su, C.-Y. A CsPbBr3 Perovskite Quantum Dot/Graphene Oxide Composite For Photocatalytic CO2 Reduction. *J. Am. Chem. Soc.* **2017**, *139*, 5660−5663.

(4) Kumar, P.; Patel, M.; Park, C.; Han, H.; Jeong, B.; Kang, H.; Patel, R.; Koh, W.-G.; Park, C. Highly Luminescent Biocompatible CsPbBr3@SiO2 Core−Shell Nanoprobes for Bioimaging and Drug Delivery. *J. Mater. Chem. B* **2020**, *8*, 10337−10345.

(5) Wang, X.; Abbasi, S.; Zhang, D.; Wang, J.; Wang, Y.; Cheng, Z.; Liu, H.; Shen, W. Electrochemical Deposition of CsPbBr3 Perovskite for Photovoltaic Devices with Robust Ambient Stability. *ACS Appl. Mater. Interfaces* **2020**, *12*, 50455−50463.

(6) Zhang, J.; Zhang, L.; Cai, P.; Xue, X.; Wang, M.; Zhang, J.; Tu, G. Enhancing Stability of Red Perovskite Nanocrystals Through Copper Substitution for Efficient Light-Emitting Diodes. *Nano Energy* **2019**, *62*, 434−441.
(7) Pathak, S.; Sakai, N.; Rivarola, F. W. R.; Stranks, S. D.; Liu, J.; Eperon, G. E.; Ducati, C.; Wojciechowski, K.; Griffiths, J. T.; Haghighirad, A. A.; et al. Perovskite Crystals for Tunable White Light Emission. *Chem. Mater.* **2015**, *27*, 8066−8075.
(8) Cheng, R.; Li, F.; Zhang, J.; She, X.; Zhang, Y.; Shao, K.; Lin, Y.; Wang, C.-F.; Chen, S. Fabrication of Amphiphilic Quantum Dots Towards High-Colour-Quality Light-Emitting Devices. *J. Mater. Chem. C* **2019**, *7*, 4244−4249.
(9) Wu, H.; Zhang, W.; Wu, J.; Chi, Y. A Visual Solar UV Sensor Based on Paraffin-Perovskite Quantum Dot Composite Film. *ACS Appl. Mater. Interfaces* **2019**, *11*, 16713−16719.
(10) Liu, Y.; Tang, X.; Zhu, T.; Deng, M.; Ikechukwu, I. P.; Huang, W.; Yin, G.; Bai, Y.; Qu, D.; Huang, X.; Qiu, F. All-Inorganic CsPbBr3 Perovskite Quantum Dots as a Photoluminescent Probe for Ultrasensitive Cu2+ Detection. *J. Mater. Chem. C* **2018**, *6*, 4793−4799.
(11) Gao, Y.; Pan, X.; Xu, S.; Liu, Z.; Wang, J.; Yu, K.; Wang, C.; Yuan, H.; Wu, S. Fluorescence-Enhanced Microfluidic Sensor for Highly Sensitive In-Situ Detection of Copper Ions in Lubricating Oil. *Mater. Des.* **2020**, *191*, No. 108693.
(12) Chowdhury, F. A.; Pradhan, B.; Ding, Y.; Towers, A.; Gesquiere, A.; Tetard, L.; Thomas, J. Perovskite Quantum Dot-Reduced Graphene Oxide Superstructure for Efficient Photodetection. *ACS Appl. Mater. Interfaces* **2020**, *12*, 45165−45173.
(13) Lin, J.; Yang, C.; Huang, P.; Wang, S.; Liu, M.; Jiang, N.; Chen, D. Photoluminescence Tuning from Glass-Stabilized CsPbX3 (X = Cl, Br, I) Perovskite Nanocrystals Triggered by Upconverting Tm: KYb2F7 Nanoparticles for High-Level Anti-Counterfeiting. *Chem. Eng. J.* **2020**, *395*, No. 125214.
(14) Lin, J.; Lu, Y.; Li, X.; Huang, F.; Yang, C.; Liu, M.; Jiang, N.; Chen, D. Perovskite Quantum Dots Glasses Based Backlit Displays. *ACS Energy Lett.* **2021**, *6*, 519−528.
(15) Bodnarchuk, M. I.; Boehme, S. C.; ten Brinck, S.; Bernasconi, C.; Shynkarenko, Y.; Krieg, F.; Widmer, R.; Aeschlimann, B.; Günther, D.; Kovalenko, M. V.; Infante, I. Rationalizing and Controlling the Surface Structure and Electronic Passivation of Cesium Lead Halide Nanocrystals. *ACS Energy Lett.* **2019**, *4*, 63−74.
(16) Sun, Q.; Wang, S.; Zhao, C.; Leng, J.; Tian, W.; Jin, S. Excitation-Dependent Emission Color Tuning from an Individual Mn-Doped Perovskite Microcrystal. *J. Am. Chem. Soc.* **2019**, *141*, 20089−20096.
(17) Li, J.; Chen, J.; Xu, L.; Liu, S.; Lan, S.; Li, X.; Song, J. A Zinc Non-Halide Dopant Strategy Enables Efficient Perovskite CsPbI3 Quantum Dot-Based Light-Emitting Diodes. *Mater. Chem. Front.* **2020**, *4*, 1444−1453.
(18) Li, Y.; Zhou, S.; Xiong, Z.; Qin, M.; Liu, K.; Cai, G.; Wang, H.; Zhao, S.; Li, G.; Hsu, Y.-J.; et al. Size Modulation and Heterovalent Doping Facilitated Hybrid Organic and Perovskite Quantum Dot Bulk Heterojunction Solar Cells. *ACS Appl. Energy Mater.* **2020**, *3*, 11359−11367.
(19) Guo, Y.; Su, J.; Wang, L.; Lin, Z.; Hao, Y.; Chang, J. Improved Doping and Optoelectronic Properties of Zn-Doped CsPbBr3 Perovskite through Mn Codoping Approach. *J. Phys. Chem. Lett.* **2021**, *12*, 3393−3400.
(20) Wang, Y.; Cao, S.; Li, J.; Li, H.; Yuan, X.; Zhao, J. Improved Ultraviolet Radiation Stability of Mn2+-Doped CsPbCl3 Nanocrystals via B-site Sn doping. *CrystEngComm* **2019**, *21*, 6238−6245.
(21) Liu, M.; Jiang, N.; Huang, H.; Lin, J.; Huang, F.; Zheng, Y.; Chen, D. Ni2+-Doped CsPbI3 Perovskite Nanocrystals With Near-Unity Photoluminescence Quantum Yield and Superior Structure Stability for Red Light-Emitting Devices. *Chem. Eng. J.* **2021**, *413*, No. 127547.
(22) Liu, Z.; Hu, M.; Du, J.; Shi, T.; Wang, Z.; Zhang, Z.; Hu, Z.; Zhan, Z.; Chen, K.; Liu, W.; et al. Subwavelength-Polarized Quasi-Two-Dimensional Perovskite Single-Mode Nanolaser. *ACS Nano* **2021**, *15*, 6900−6908.
(23) Chen, Z.; Zhou, B.; Yuan, J.; Tang, N.; Lian, L.; Qin, L.; Zhu, L.; Zhang, J.; Chen, R.; Zang, J. Cu2+-Doped CsPbI3 Nanocrystals with Enhanced Stability for Light-Emitting Diodes. The. *J. Phys. Chem. Lett.* **2021**, *12*, 3038−3045.
(24) Ju, D.; Jiang, X.; Xiao, H.; Chen, X.; Hu, X.; Tao, X. Narrow Bandgap and High Mobility of Lead-Free Perovskite Single Crystal Sn-doped MA3Sb2I9. *J. Mater. Chem. A* **2018**, *6*, 20753−20759.
(25) Behera, R. K.; Dutta, A.; Ghosh, D.; Bera, S.; Bhattacharyya, S.; Pradhan, N. Doping the Smallest Shannon Radii Transition Metal Ion Ni (II) for Stabilizing α-CsPbI3 Perovskite Nanocrystals. The. *J. Phys. Chem. Lett.* **2019**, *10*, 7916−7921.
(26) Protesescu, L.; Yakunin, S.; Bodnarchuk, M. I.; Krieg, F.; Caputo, R.; Hendon, C. H.; Yang, R. X.; Walsh, A.; Kovalenko, M. V. Nanocrystals of Cesium Lead Halide Perovskites (CsPbX3, X= Cl, Br, and I): Novel Optoelectronic Materials Showing Bright Emission With Wide Color Gamut. *Nano Lett.* **2015**, *15*, 3692−3696.
(27) Chen, D.; Chen, X. Luminescent Perovskite Quantum Dots: Synthesis, Microstructures, Optical Properties and Applications. *J. Mater. Chem. C* **2019**, *7*, 1413−1446.
(28) Zhao, Y.; Li, J.; Dong, Y.; Song, J. Synthesis of Colloidal Halide Perovskite Quantum Dots/Nanocrystals: Progresses and Advances. *Isr. J. Chem.* **2019**, *59*, 649−660.
(29) Yassitepe, E.; Yang, Z.; Voznyy, O.; Kim, Y.; Walters, G.; Castañeda, J. A.; Kanjanaboos, P.; Yuan, M.; Gong, X.; Fan, F.; et al. Amine-Free Synthesis of Cesium Lead Halide Perovskite Quantum Dots for Efficient Light-Emitting Diodes. *Adv. Funct. Mater.* **2016**, *26*, 8757−8763.
(30) Hu, Z.; Liu, Z.; Zhan, Z.; Shi, T.; Du, J.; Tang, X.; Leng, Y. Advances in Metal Halide Perovskite Lasers: Synthetic Strategies, Morphology Control, and Lasing Emission. *Adv. Photonics* **2021**, *3*, No. 034002.
(31) Wang, X.; Bao, Z.; Chang, Y.-C.; Liu, R.-S. Perovskite Quantum Dots for Application in High Color Gamut Backlighting Display of Light-Emitting Diodes. *ACS Energy Lett.* **2020**, *5*, 3374−3396.
(32) Liu, H.; Wu, Z.; Gao, H.; Shao, J.; Zou, H.; Yao, D.; Liu, Y.; Zhang, H.; Yang, B. One-Step Preparation of Cesium Lead Halide CsPbX3 (X= Cl, Br, and I) Perovskite Nanocrystals by Microwave Irradiation. *ACS Appl. Mater. Interfaces* **2017**, *9*, 42919−42927.
(33) Pan, H.; Li, X.; Zhang, X.; Liu, J.; Chen, X.; Zhang, H.; Huang, A.; Xiao, Z. Effect of Oleamine on Microwave-Assisted Synthesis of Cesium Lead Bromide Perovskite Nanocrystals. *Langmuir* **2020**, *36*, 13663−13669.
(34) Thapa, S.; Bhardwaj, K.; Basel, S.; Pradhan, S.; Eling, C. J.; Adawi, A. M.; Bouillard, J.-S. G.; Stasiuk, G. J.; Reiss, P.; Pariyar, A.; Tamang, S. Long-Term Ambient Air-Stable Cubic CsPbBr3 Perovskite Quantum Dots Using Molecular Bromine. *Nanoscale Adv.* **2019**, *1*, 3388−3391.
(35) Gaulding, E. A.; Chen, X.; Yang, Y.; Harvey, S. P.; To, B.; Kim, Y.-H.; Beard, M. C.; Sercel, P. C.; Luther, J. M. Embedding PbS Quantum Dots (QDs) in Pb-Halide Perovskite Matrices: QD Surface Chemistry and Antisolvent Effects on QD Dispersion and Confinement Properties. *ACS Mater. Lett.* **2020**, *2*, 1464−1472.
(36) Ren, J.; Li, T.; Zhou, X.; Dong, X.; Shorokhov, A. V.; Semenov, M. B.; Krevchik, V. D.; Wang, Y. Encapsulating All-Inorganic Perovskite Quantum Dots into Mesoporous Metal Organic Frameworks With Significantly Enhanced Stability for Optoelectronic Applications. *Chem. Eng. J.* **2019**, *358*, 30−39.
(37) Jia, C.; Li, H.; Meng, X.; Li, H. CsPbX3/Cs4PbX6 Core/Shell Perovskite Nanocrystals. *Chem. Commun.* **2018**, *54*, 6300−6303.
(38) Lou, S.; Zhou, Z.; Xuan, T.; Li, H.; Jiao, J.; Zhang, H.; Gautier, R.; Wang, J. Chemical Transformation of Lead Halide Perovskite into Insoluble, Less Cytotoxic, and Brightly Luminescent CsPbBr3/CsPb2Br5 Composite Nanocrystals for Cell Imaging. *ACS Appl. Mater. Interfaces* **2019**, *11*, 24241−24246.
(39) Hu, Z.; Liu, Z.; Bian, Y.; Li, S.; Tang, X.; Du, J.; Zang, Z.; Zhou, M.; Hu, W.; Tian, Y.; Leng, Y. Enhanced Two-Photon-Pumped Emission from In Situ Synthesized Nonblinking CsPbBr3/SiO2

https://doi.org/10.1021/acsami.1c19644
ACS Appl. Mater. Interfaces 2022, 14, 278−296

Nanocrystals with Excellent Stability. *Adv. Opt. Mater.* **2018**, *6*, No. 1700997.
(40) Park, H.; Na, K. Conjugation of the Photosensitizer Chlorin e6 to Pluronic F127 for Enhanced Cellular Internalization for Photodynamic Therapy. *Biomaterials* **2013**, *34*, 6992−7000.
(41) Getachew, G.; Huang, W.-W.; Chou, T.-H.; Rasal, A. S.; Chang, J.-Y. Brightly Luminescent (NH4)xCs1-xPbBr3 Quantum Dots for In Vitro Imaging and Efficient Photothermal Ablation Therapy. *J. Colloid Interface Sci.* **2022**, *605*, 500−512.
(42) Swarnkar, A.; Mir, W. J.; Nag, A. Can B-site Doping or Alloying Improve Thermal-and Phase-stability of All-Inorganic CsPbX3 (X = Cl, Br, I) Perovskites? *ACS Energy Lett.* **2018**, *3*, 286−289.
(43) Shen, X.; Zhang, Y.; Kershaw, S. V.; Li, T.; Wang, C.; Zhang, X.; Wang, W.; Li, D.; Wang, Y.; Lu, M.; et al. Zn-alloyed CsPbI3 Nanocrystals for Highly Efficient Perovskite Light-Emitting Devices. *Nano Lett.* **2019**, *19*, 1552−1559.
(44) Cai, T.; Yang, H.; Hills-Kimball, K.; Song, J.-P.; Zhu, H.; Hofman, E.; Zheng, W.; Rubenstein, B. M.; Chen, O. Synthesis of All-Inorganic Cd-Doped CsPbCl3 Perovskite Nanocrystals With Dual-Wavelength Emission. The. *J. Phys. Chem. Lett.* **2018**, *9*, 7079−7084.
(45) Pan, G.; Bai, X.; Xu, W.; Chen, X.; Zhai, Y.; Zhu, J.; Shao, H.; Ding, N.; Xu, L.; Dong, B.; et al. Bright Blue Light Emission of Ni2+ ion-Doped CsPbClxBr3−x Perovskite Quantum Dots Enabling Efficient Light-Emitting Devices. *ACS Appl. Mater. Interfaces* **2020**, *12*, 14195−14202.
(46) Bi, C.; Sun, X.; Huang, X.; Wang, S.; Yuan, J.; Wang, J. X.; Pullerits, Tn.; Tian, J. Stable CsPb1−xZnxI3 Colloidal Quantum Dots with Ultralow Density of Trap States for High-Performance Solar Cells. *Chem. Mater.* **2020**, *32*, 6105−6113.
(47) Zhou, Y.; Zhou, D.-D.; Liu, B.-M.; Li, L.-N.; Yong, Z.-J.; Xing, H.; Fang, Y.-Z.; Hou, J.-S.; Sun, H.-T. Ultrabroad Near-Infrared Photoluminescence from Bismuth Doped CsPbI3: Polaronic Defects vs. Bismuth Active Centers. *J. Mater. Chem. C* **2016**, *4*, 2295−2301.
(48) Krieg, F.; Ochsenbein, S. T.; Yakunin, S.; ten Brinck, S.; Aellen, P.; Süess, A.; Clerc, B.; Guggisberg, D.; Nazarenko, O.; Shynkarenko, Y.; et al. Colloidal CsPbX3 (X = Cl, Br, I) Nanocrystals 2.0: Zwitterionic Capping Ligands for Improved Durability and Stability. *ACS Energy Lett.* **2018**, *3*, 641−646.
(49) Zhang, X.; Bai, X.; Wu, H.; Zhang, X.; Sun, C.; Zhang, Y.; Zhang, W.; Zheng, W.; Yu, W. W.; Rogach, A. L. Water-Assisted Size and Shape Control of CsPbBr3 Perovskite Nanocrystals. *Angew. Chem., Int. Ed.* **2018**, *57*, 3337−3342.
(50) Tang, X.; Chen, W.; Liu, Z.; Du, J.; Yao, Z.; Huang, Y.; Chen, C.; Yang, Z.; Shi, T.; Hu, W.; et al. Ultrathin, Core−Shell Structured SiO2 Coated Mn2+-Doped Perovskite Quantum Dots for Bright White Light-Emitting Diodes. *Small* **2019**, *15*, No. 1900484.
(51) Li, D.; Li, X.; Zhao, T.; Liu, H.; Jiang, S.; Zhang, Q.; Ågren, H.; Chen, G. Ultraefficient Singlet Oxygen Generation from Manganese-Doped Cesium Lead Chloride Perovskite Quantum Dots. *ACS Nano* **2020**, *14*, 12596−12604.
(52) Wang, H.; Zhuang, J.; Velado, D.; Wei, Z.; Matsui, H.; Zhou, S. Near-Infrared-and Visible-Light-Enhanced Metal-Free Catalytic Degradation of Organic Pollutants Over Carbon-Dot-Based Carbocatalysts Synthesized from Biomass. *ACS Appl. Mater. Interfaces* **2015**, *7*, 27703−27712.
(53) Liu, H.; Wang, H.; Qian, Y.; Zhuang, J.; Hu, L.; Chen, Q.; Zhou, S. Nitrogen-Doped Graphene Quantum Dots as Metal-Free Photocatalysts for Near-Infrared Enhanced Reduction of 4-Nitrophenol. *ACS Appl. Nano Mater.* **2019**, *2*, 7043−7050.
(54) Yousefi, R.; Beheshtian, J.; Seyed-Talebi, S. M.; Azimi, H.; Jamali-Sheini, F. Experimental and Theoretical Study of Enhanced Photocatalytic Activity of Mg-doped ZnO NPs and ZnO/rGO Nanocomposites. *Chem. − Asian J.* **2018**, *13*, 194−203.
(55) Pradeev raj, K.; Kennedy, A.; Sagadevan, S.; Chowdhury, Z. Z.; Johan, M. R. B.; Aziz, F. A.; Rafique, R. F.; Selvi, R. T.; et al. Influence of Mg doping on ZnO Nanoparticles for Enhanced Photocatalytic Evaluation and Antibacterial Analysis. *Nanoscale Res. Lett.* **2018**, *13*, No. 229.
(56) Huang, C.-L.; Huang, C.-C.; Mai, F.-D.; Yen, C.-L.; Tzing, S.-H.; Hsieh, H.-T.; Ling, Y.-C.; Chang, J.-Y. Application of Paramagnetic Graphene Quantum Dots as a Platform for Simultaneous Dual-Modality Bioimaging and Tumor-Targeted Drug Delivery. *J. Mater. Chem. B* **2015**, *3*, 651−664.
(57) Yao, Y.-Y.; Gedda, G.; Girma, W. M.; Yen, C.-L.; Ling, Y.-C.; Chang, J.-Y. Magnetofluorescent Carbon Dots Derived from Crab Shell for Targeted Dual-Modality Bioimaging and Drug Delivery. *ACS Appl. Mater. Interfaces* **2017**, *9*, 13887−13899.
(58) Robertson, A. G.; Rendina, L. M. Gadolinium Theranostics for the Diagnosis and Treatment of Cancer. *Chem. Soc. Rev.* **2021**, *50*, 4231−4244.
(59) Qian, X.; Han, X.; Yu, L.; Xu, T.; Chen, Y. Manganese-Based Functional Nanoplatforms: Nanosynthetic Construction, Physiochemical Property, and Theranostic Applicability. *Adv. Funct. Mater.* **2020**, *30*, No. 1907066.
(60) Mauri, M.; Collico, V.; Morelli, L.; Das, P.; García, I.; Penaranda Avila, J.; Bellini, M.; Rotem, R.; Truffi, M.; Corsi, F.; Simonutti, R.; Liz-Marzán, L. M.; Colombo, M.; Prosperi, D. MnO Nanoparticles Embedded in Functional Polymers as T1 Contrast Agents for Magnetic Resonance Imaging. *ACS Appl. Nano Mater.* **2020**, *3*, 3787−3797.
(61) Getachew, G.; Korupalli, C.; Rasal, A. S.; Chang, J.-Y. ROS Generation/Scavenging Modulation of Carbon Dots as Phototherapeutic Candidates and Peroxidase Mimetics to Integrate with Polydopamine Nanoparticles/GOx Towards Cooperative Cancer Therapy. *Composites, Part B* **2021**, *226*, No. 109364.

https://doi.org/10.1021/acsami.1c19644
ACS Appl. Mater. Interfaces 2022, 14, 278−296

ACS APPLIED MATERIALS & INTERFACES

Editor-in-Chief:
Kirk S. Schanze

About the Journal

Open Access
Submission & Review

Submit Manuscript

Editors & Editorial Board

Editor-in-Chief

Kirk S. Schanze
University of Texas Health Science Center at San Antonio
United States
E-mail: eic@ami.acs.org

Current Issue Editorial Masthead

View the Masthead in Current Issue

Executive Editors

Omar Farha
Northwestern University
United States
E-mail: farha-office@ami.acs.org

Ellen R. Fisher
Colorado State University
United States
E-mail: fisher-office@ami.acs.org

Albena Ivanisevic
North Carolina State University
United States
E-mail: ivanisevic-office@ami.acs.org

Peter Müller-Buschbaum
Technische Universität München
Germany
E-mail: muellerb-office@ami.acs.org

Osvaldo N. Oliveira Jr.
University of São Paulo Institute of Physics
Brazil
E-mail: oliveira-office@ami.acs.org

Vladimir V. Tsukruk
Georgia Institute of Technology
United States
E-mail: tsukruk-office@ami.acs.org

Stanislaus Wong
Stony Brook University Department of Biochemistry and Cell Biology
United States
E-mail: wong-office@ami.acs.org

Yiying Wu
Ohio State University
United States
E-mail: wu-office@ami.acs.org

United States
E-mail: bardhan-office@ami.acs.org

David Beljonne
University of Mons
Belgium
E-mail: beljonne-office@ami.acs.org

Rabah Boukherroub
IEMN
France
E-mail: boukherrob@ami.acs.org

Mary B. Chan-Park
Nanyang Technological University
Singapore
E-mail: chan-park-office@ami.acs.org

Sing Yian Chew
Nanyang Technological University
Singapore
E-mail: chew-office@ami.acs.org

Nam-Soon Choi
Korea Advanced Institute of Science and Technology
Republic of Korea
E-mail: choi-office@ami.acs.org

Pi-Tai Chou
National Taiwan University
Taiwan
E-mail: chou-office@ami.acs.org

Akhilesh K. Gaharwar
Texas A&M University
United States
E-mail: gaharwar-office@ami.acs.org

Yu-Guo Guo
Institute of Chemistry Chinese Academy of Sciences
China
E-mail: ygg-office@ami.acs.org

United States
E-mail: hamann-office@ami.acs.org

Yan Yan Sherry Huang
University of Cambridge
United Kingdom
E-mail: huang-office@ami.acs.org

Fengwei Huo
Nanjing Tech University
China
E-mail: huo-office@ami.acs.org

Jesse V. Jokerst
University of California San Diego
United States
E-mail: jokerst-office@ami.acs.org

Sang Hoon Joo
Seoul National University
Republic of Korea
E-mail: joo-office@ami.acs.org

Holger Kleinke
University of Waterloo
Canada
E-mail: kleinke-office@ami.acs.org

Weiyang Li
Dartmouth College
United States
E-mail: li-office@ami.acs.org

Jun Lu
Argonne National Laboratory
United States
E-mail: lu-office@ami.acs.org

Zhengtang Tom Luo
The Hong Kong University of Science and Technology
China
E-mail: luo-office@ami.acs.org

United States
E-mail: managing-editor@ami.acs.org

Coordinating Editor

Barbara M. Schanze
E-mail: eic@ami.acs.org

Editorial Advisory Board

Okinawa Institute of Science and Technology Graduate University
Japan

Lisa McElwee-White
University of Florida
United States

Yoshiko Miura
Kyushu University
Japan

Satish Ogale
CSIR-National Chemical Laboratory
India

Selina Olthof
Universitat zu Koln Department fur Chemie
Germany

Catia Ornelas
Universidade Estadual de Campinas
Brazil

Emily Pentzer
Texas A&M University
United States

C. Retna Raj
IIT Kharagpur
India

John R. Reynolds
Georgia Institute of Technology
United States

Svetlana Santer
University of Potsdam Institute of Physics and Astronomy
Germany

Jessica D. Schiffman
University of Massachusetts Amherst
United States

Qing Shen
The University of Electro-Communications
Japan

Texas A&M University
United States

Sabine Szunerits
University of Lille
France

Yanli Tang
Shaanxi Normal University
China

Xiaolin Wang
University of Wollongong
Australia

Luisa Whittaker-Brooks
University of Utah
United States

John Wilson
Vanderbilt University
United States

Ken-Tsung Wong
National Taiwan University
Taiwan

Chung-Chih Wu
National Taiwan University
Taiwan

Yun Yan
Peking University
China

Juyoung Yoon
Ewha Womans University
Republic of Korea

Ya You
Wuhan Institute of Technology
China

Zhong-Zhen Yu
Beijing University of Chemical Technology
China

University of Heidelberg
Germany

Xi'an Jiaotong University
China

Partners

ACS applied materials & interfaces

COUNTRY

United States

Universities and research institutions in United States

Media Ranking in United States

SUBJECT AREA AND CATEGORY

Materials Science
- Materials Science (miscellaneous)
- Nanoscience and Nanotechnology

Medicine
- Medicine (miscellaneous)

PUBLISHER

American Chemical Society

American Chemical Society in Scimago Institutions Rankings

H-INDEX

284

PUBLICATION TYPE

Journals

ISSN

19448252, 19448244

COVERAGE

2009-2022

INFORMATION

Homepage

How to publish in this journal

eic@ami.acs.org

SCOPE

ACS Applied Materials & Interfaces serves the interdisciplinary community of chemists, engineers, physicists and biologists focusing on how newly-discovered materials and interfacial processes can be developed and used for specific applications. The editors are proud of the rapid growth of the journal since its inception in 2009, both in terms of the number of published articles and the impact of the research reported in those articles. ACS AMI is also truly international, with the majority of published articles now coming from outside the United States, capturing the rapid growth in applied research around the globe. The following journal TOC sections provide a high-level guide to the journal scope: -Biological and medical applications of materials and interfaces- Energy, environmental, and catalysis applications- Functional inorganic materials and devices- Organic electronic

devices- Functional nanostructured materials (including low-d carbon)- Applications of polymer, composite, and coating materials- Surfaces, interfaces, and applications.

Join the conversation about this journal

Quartiles

FIND SIMILAR JOURNALS

1	2	3	4
Advanced Materials Interfaces	**Materials Horizons**	**Small**	**Science China M**
GBR	GBR	DEU	CHN
94% similarity	**91%** similarity	**90%** similarity	**89** simila

SJR

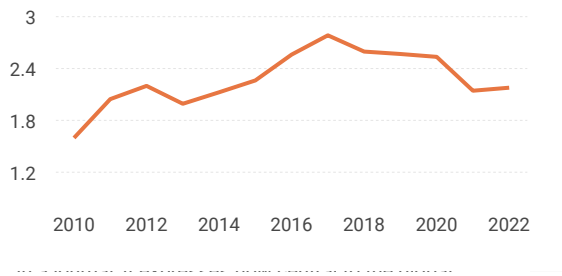

Total Documents

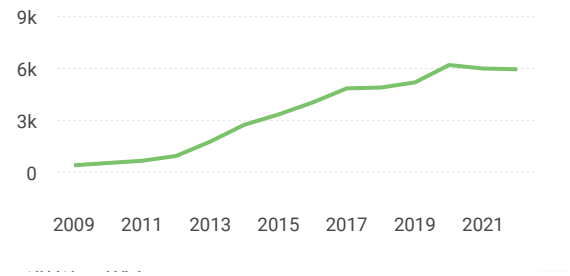

Total Cites Self-Cites

Citations per document

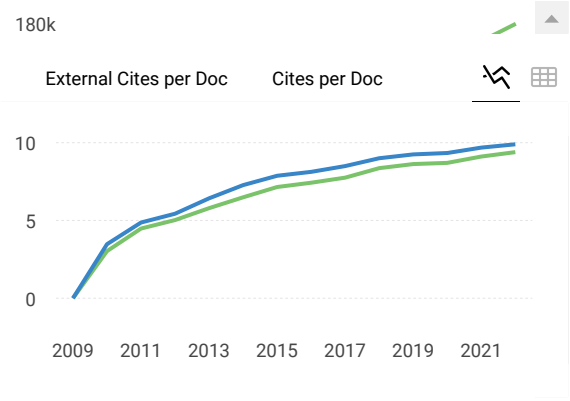

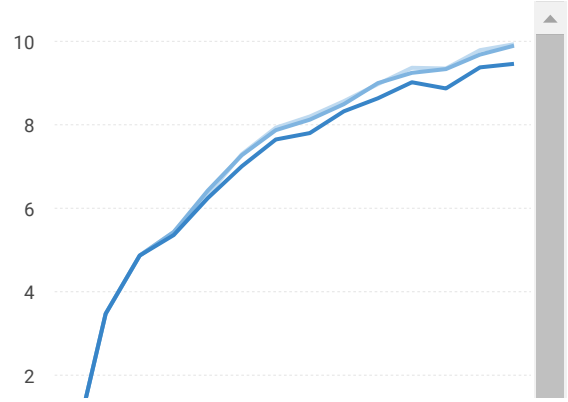

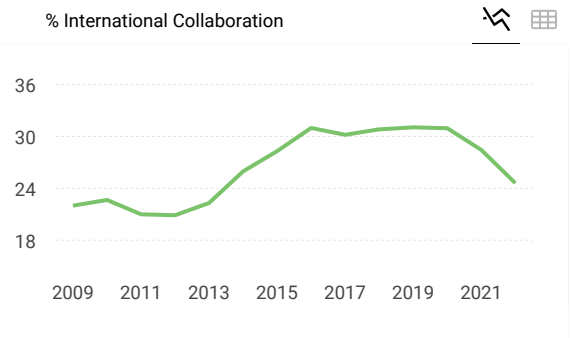

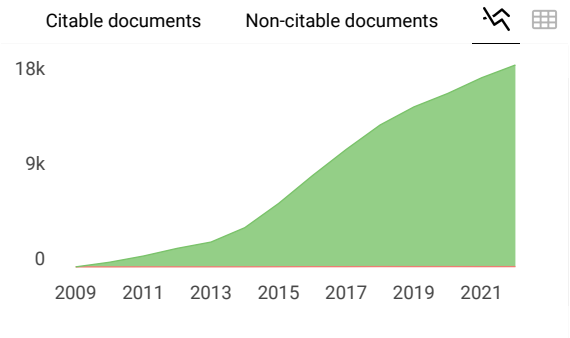

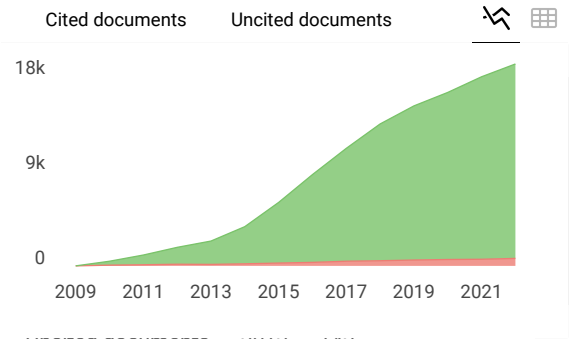

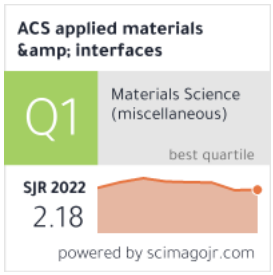

← Show this widget in your own website

Just copy the code below and paste within your html code:

```
<a href="https://www.scimag
```

SCImago Graphica

Explore, visually communicate and make sense of data with our **new data visualization tool**.

Metrics based on Scopus® data as of April 2023

A **ahmed medhat** 2 years ago

I need to know the impact factor of ACS applied electronic materials

reply

SCImago Team

Melanie Ortiz 2 years ago

Dear Ahmed, thank you very much for your comment. SCImago Journal and Country Rank uses Scopus data, our impact indicator is the SJR (Check it on our website). We suggest you consult the Journal Citation Report for other indicators (like Impact Factor) with a Web of Science data source. Best Regards, SCImago Team

W **WALID** 3 years ago

I need know what impact factor of ACS Applied Materials

reply

S **Shatil Shahriar** 3 years ago

It is 8.47

SCImago Team

Melanie Ortiz 3 years ago

Dear Walid, thank you very much for your comment.
SCImago Journal and Country Rank uses Scopus data, our impact indicator is the SJR. Check out our web to localize the journal. We suggest you to consult the Journal Citation Report for other indicators (like Impact Factor) with a Web of Science data source. Best Regards, SCImago Team

Leave a comment

Name

Email
(will not be published)

I'm not a robot reCAPTCHA

Submit

The users of Scimago Journal & Country Rank have the possibility to dialogue through comments linked to a specific journal. The purpose is to have a forum in which general doubts about the processes of publication in the journal, experiences and other issues derived from the publication of papers are resolved. For topics on particular articles, maintain the dialogue through the usual channels with your editor.

Source details

ACS applied materials & interfaces

Open Access

Scopus coverage years: from 2009 to Present

Publisher: American Chemical Society

ISSN: 1944-8244 E-ISSN: 1944-8252

Subject area: Materials Science: General Materials Science

Source type: Journal

CiteScore 2021
14.4

SJR 2021
2.143

SNIP 2021
1.407

View all documents > | Set document alert | Save to source list

CiteScore | CiteScore rank & trend | Scopus content coverage

Improved CiteScore methodology

CiteScore 2021 counts the citations received in 2018-2021 to articles, reviews, conference papers, book chapters and data papers published in 2018-2021, and divides this by the number of publications published in 2018-2021. Learn more >

CiteScore 2021

$$14.4 = \frac{309{,}438 \text{ Citations 2018 - 2021}}{21{,}423 \text{ Documents 2018 - 2021}}$$

Calculated on 05 May, 2022

CiteScoreTracker 2022

$$15.7 = \frac{335{,}830 \text{ Citations to date}}{21{,}409 \text{ Documents to date}}$$

Last updated on 05 April, 2023 • Updated monthly

CiteScore rank 2021

Category	Rank	Percentile
Materials Science └ General Materials Science	#33/455	92nd

View CiteScore methodology > | CiteScore FAQ > | Add CiteScore to your site

About Scopus

What is Scopus

Content coverage

Scopus blog

Scopus API

Privacy matters

Language

日本語版を表示する

查看简体中文版本

查看繁體中文版本

Просмотр версии на русском языке

Customer Service

Help

Tutorials

Contact us